Pick & Place Integration of Diamond Nanophotonic Structures for Modular, On Chip Diamond Quantum Systems

Saliha Neji

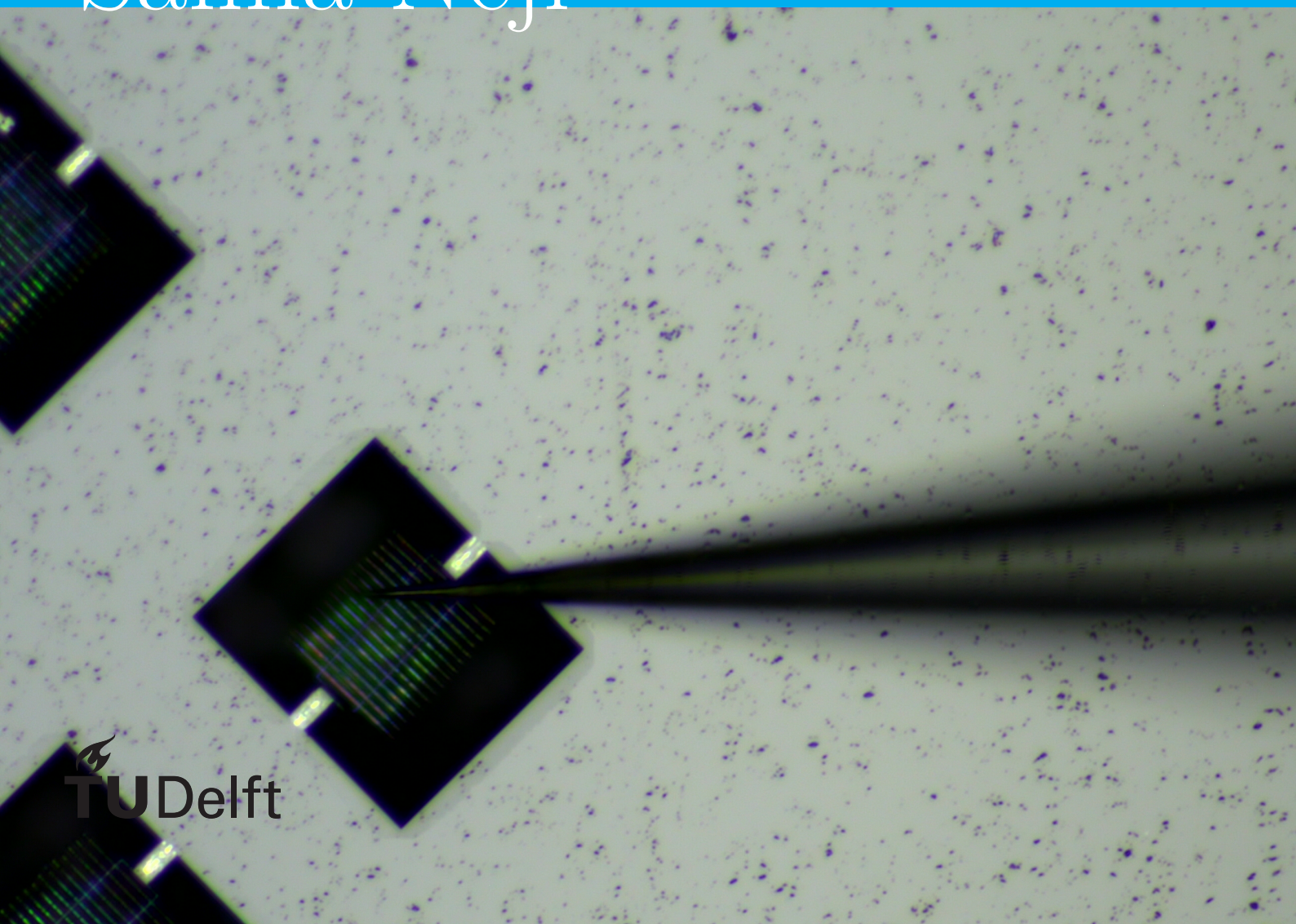

TUDelft

Pick & Place Integration of Diamond Nanophotonic Structures for Modular, On Chip Diamond Quantum Systems

by

Saliha Neji

A Thesis
Submitted to the Faculty of Electrical Engineering, Mathematics and Computer Science
Delft University of Technology
for the Degree of Master of Science
April 3^{rd} 2023

Promotors:	Prof. Dr. Ryoichi Ishihara
	Prof. Dr. Lina Sarro
	Prof. Dr. Ronald Hanson
Supervisors:	Prof. Dr. Ryoichi Ishihara
	Alan Yu
	Dr. Salahuddin Nur

TU Delft

Contents

Abstract

Diamond color centers have been increasingly gaining attention in research due to their desirable optical properties that make them suitable for applications such as quantum computing, quantum sensing and quantum communication. However, the main challenge has been on-chip integration of diamond color centers with high scalability and high yield. Many diamond integration methods have been researched, such as heterogeneous wafer bonding of diamond-on-insulator photonics. While this method offers high scalability and wafer level fabrication, optical performance is not guaranteed due to the non-ideal processing which results in lower yield. Another integration method is pick and place, which demonstrated high yield as the diamond color centers can be pre-selected before integration, and thus resulting in higher yield. Here, pick and place integration of diamond nano-photonic structures is presented. For that purpose, an adiabatic coupler is designed, with simulation results showing $0.36dB$ insertion loss and 3dB misalignment tolerance of $180nm$ and $5\mu m$ in x and z directions respectively. A mechanical support structure is designed such that optical losses at that interface are minimized. The simulated loss is reduced from 33% to only 4% and the cross-talk is $-11dB$. Further optical measurement is needed to determine the achieved transmission of the integrated diamond chiplets. Finally, pick and place is performed with 6 different supporting structure designs. The yield is 25% with minimum misalignment of $50nm$ which is mainly dominated by random motion of the diamond chiplet as it gets closer to the receptor chip. This random motion is attributed to the surface roughness of the receptor chip and and lower surface of the diamond chiplet. In addition, residual charges in both chips results in Coulomb forces acting on the diamond chiplet and thus contributing to the misalignment. It is expected that the magnitude of the random motion, and consequently, the misalignment, will be improved by treating the receptor chip surface with HMDS and de-ionizing both the diamond chiplet and the receptor chip.

1

Introduction

1.1. Diamond defects

Defects in diamonds either occur naturally or are created by an impurity atom, typically nitrogen, replacing a carbon atom in the diamond crystal lattice. The nitrogen impurity atom bonds with the carbon atoms in the crystal lattice, while creating a vacancy in the adjacent lattice. The nitrogen atom covalently bonds with the neighboring carbon atoms while leaving unbonded electrons as shown in fig. 1.2 a. These unpaired electrons can be then controlled and manipulated to be able to use them in various applications such as quantum computation, quantum emission and quantum sensing.

1.1.1. Diamond defects for quantum computation

The basic principle of quantum computation is to encode information in a quantum state which can be controlled externally to perform a desired computation. A good candidate is a quantum states that can be distinguished from other states, and that is sufficiently sensitive to external drive, such as optical drive, magnetic fields, etc.

The unpaired electrons in the NV center can be utilized for that purpose. The total electron spin in the NV center is S=1 which is a superposition of the degenerate spin states $m_s = -1, 0, 1$ (see fig. 1.1), i.e. spin states with the same energy [1]. The degeneracy of the states $m_s = 0$ and $m_s = \pm 1$ is lifted via the zero-field splitting D_0, which results from the hyperfine-interaction between the electrons and the electrons with the nuclei. As for the degeneracy of the spin states $m_s = 1$ and $m_s = -1$, it is lifted as a result of an externally applied magnetic field. This is called the Zeeman effect and the splitting between the states is proportional to $2\gamma_{NV} B_{NV}$ where γ_{NV} is the gyromagnetic ratio of electron and B_{NV} is the applied magnetic field in the z-axis, parallel to the spin. Figure 1.1 illustrates the resulting energy levels.

The splitting in the degenerate states allows to define a qubit. In this case, the states $m_s = 0$ and $m_s = -1$ form a two-level system where the qubit states $|0\rangle$ and $ket1$ are defined respectively. The transition from the ground state to the excited state occurs via optical transitions. This is achieved by shining laser on the NV center, and when the frequency of the laser is in resonance with the optical transition frequency, then the quantum state makes transition from the ground state to the excited state. Once the spin is in the excited state, it remains there for a short time called the radiative lifetime, and then decays back to the ground state while emitting a photon in a process called spontaneous emission. This is demonstrated in [2] and shown in fig. 1.2 c. The figure illustrates the increased number of photon counts as a result of spontaneous emission when the laser is tuned in resonance with spin.

The quantum state is also subjected to fluctuations originated from the environment, such as neighboring nuclear spins that couple via hyperfine interaction and lattice vibrations i.e. phonons which mediate transitions to undesirable energy levels near the excited state. These fluctuations cause the quantum state to decohere, that is losing its encoded state and randomly transforming to some other state. This process takes a certain time which is defined as the qubit coherence time. Ideally, the coherence time has to be as long as possible to reliably perform computations before the qubit loses its state.

The qubit coherence times are characterized by T_1, the relaxation time, and T_2^*, the dephasing time.

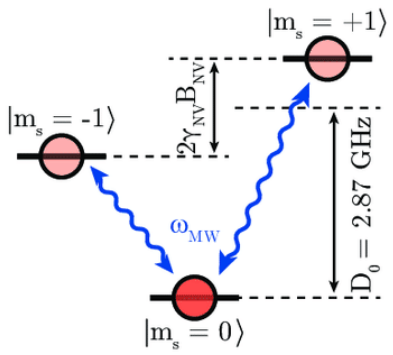

Figure 1.1: The energy levels of the spin states $m_s = 0$ and $m_s = \pm 1$ [3].

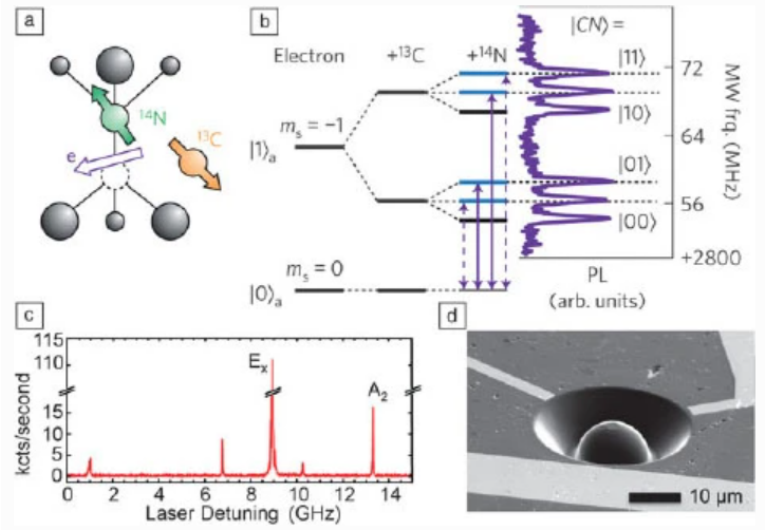

Figure 1.2: (a) Electron spin and nucleus spin of 13C and 14N atoms. (b) Qubit energy levels [1].

T_1 is a measure of how long it takes for the spin state to relax from the excited state to the ground state. Therefore, T_1 can be measured by applying a π pulse that rotates the spin from $|0\rangle$ to $|1\rangle$, and then measure the probability of the spin remaining in state $|1\rangle$ in time, denoted as $P_{|1\rangle}$. Due to decoherence, $P_{|1\rangle}$ decays exponentially in time, and therefore, T_1 is defined as the time when $P_{|1\rangle}$ decays to $\frac{1}{e}$ of its initial value.
As for the dephasing time, T_2^*, it is a measure of the time it takes for the qubit to acquire a phase large enough for it to decohere to a random state. This can be measured using the Ramsey experiment. The qubit is first initialized in $|0\rangle$ followed by a $\frac{\pi}{2}$ pulse which takes it to the superposition state $|+\rangle$ where it can acquire a phase. After some time t, another $\frac{\pi}{2}$ pulse is applied, and depending on the degree of dephasing, the qubit either rotates to $|0\rangle$ or $|1\rangle$. Therefore, T_2^* is the time at which $P_{|1\rangle}$ has decayed to $\frac{1}{e}$ of its initial value.

What makes NV centers stand out when compared to other qubits is their long coherence times, which are typically in the order of ms at room temperature [4]. This makes NV centers more practical when compared to other qubits such as superconducting qubits that need to be cooled down to cryogenic temperatures.

1.1.2. Diamond defects for quantum emission

In the previous section, we have seen that the electron spin in the NV center absorbs a photon and makes the transition to the excited state and then decays back to the ground state emitting a photon. This makes diamond defects useful as a single photon sources with very good optical properties. The optical transition of interest is the photon controlled transition, which is called the zero phonon line (ZPL). However, we have seen in the previous section that optical transitions can be mediated by phonons creating phonon-sideband states whose energy levels are quite close to the energy level of the excited state. This deteriorates the optical response of the single photon source as these transitions contribute to the total emission which can overly the ZPL. Therefore, a good single photon source is characterized by a spectrum that displays high ZPL and low phonon-side bands.

For NV centers, the ZPL is only 4% of the total emission [5], i.e. most of the emitted intensity is at wavelengths corresponding to the phonon sidebands, which makes it challenging to reliably detect the emitted photon from the NV center. This has opened the path for IV-elements color centers where the impurity atom is either Si, Ge, Sn or Pb. Since these atoms have the same number of valence electrons, they bond in the same manner with the carbon atoms in the diamond crystal and thus creating the same crystal structure [6]. Therefore, the same model can be used to understand the properties of group 4 color centers. The model is developed in [7] for SiV and has been experimentally verified in [8] for SnV. This allows for a quantitative comparison between the optical properties of group 4 color centers summarized in table 1.1.

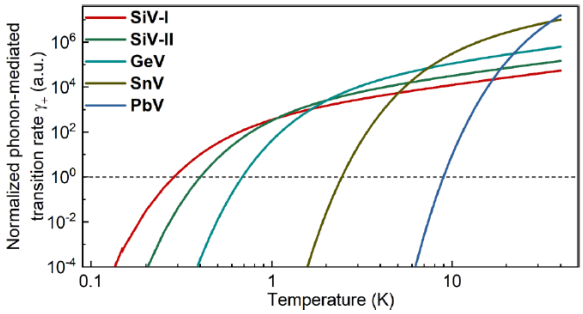

Figure 1.3: The calculated phonon mediated transition rates of the group 4 color centers as a function of temperature [13]

These group 4 color centers show promising optical properties when compared to NV centers where the ZPL emission is much higher, 70% for SiV [9] and 60% for GeV [10]. The main difference between group 4 color centers lies in the atomic number. Higher atomic number increases the splitting in the energy states as a result of higher spin-orbit coupling. The energy level splitting between the ground state and the first excited stated for the color centers can be found in table 1.1. Higher splitting in the energy levels reduces the probability with which an electron makes a photon-mediated transition to the ground state, consequently, increasing the coherence time [11]. Note that the same can be achieved by reducing the temperature, because of the reduced lattice vibrations at cryogenic temperatures, however reducing the temperature to sub-Kelvin levels is undesirable. Therefore, higher splitting allows for higher coherence times without the need to further reduce the temperature. This is further illustrated in fig. 1.3 where the phonon-mediated transition rate γ is calculated for group 4 color centers and plotted against temperature. The figure shows that for the same γ, SiV-I must operate at $0.4K$, which is slightly improved to $0.5K$ for SiV whose energy level splitting is controlled by strain tuning [12], denoted as SiV-II. Whereas PbV can operate at temperatures as high as $10K$ for the same phonon-mediated transition rate.

Another important property of quantum emitters is speed at which a single photon is emitted. This can be characterized by the radiation lifetime τ_r, which is the time during which the spin state remains in the excited state. After τ_r elapses, the state decays back to the ground state emitting a photon. Ideally, τ_r should be as short as possible to allow for a fast response.

Quantity	NV	SiV	GeV	SnV	PbV
$ZPL[nm]$	637.5 [14]	740 [15]	603 [16]	621.5 [11]	550 [13]
ZPL emission	4% [5]	70% [9]	60% [10]	-	-
$\tau_r[ns]$	12 & 7.8 [17]	1.2-1.8 [18]	6 [19]	~5 [11]	3.7 [13]
η	~1 [20]	0.6 [21]	$> \eta_{SiV}$ [19]	0.8 [11]	-
$\Delta_{gs}[meV]$	NA	0.2 [22]	0.7 [10]	3.5 [11]	16.16 [13]
$\Delta_{es}[meV]$	NA	1.07 [22]	4.5 [10]	12.4 [11]	-
T_2^*	1.8 ms (RT) [23]	10 ms (0.1 K) [24]	19 ns (2K) [25]	59 ns (6 K) [8]	-
T_1	3 ms (RT) [26]	1 s (0.1 K) [24]	25 μ s (2K) [25]	1.26 ms (6 K) [8]	-

Table 1.1: Comparison between the IV-element color centers. τ_r is the radiative lifetime where the two radiative lifetimes for NV correspond to each spin state. η is the quantum efficiency. Δ_{gs} is the splitting in the ground state and Δ_{es} is the splitting in the excited state. Note that the difference between these splittings is attributed to the Jahn-Teller effect [7]. Different PbV splitting values have been reported in the literature, one is 16.16 meV [13] and the other is 23.62 meV [27], since the calculations done in [28] predicted a value of 18.17 meV, the latter value was discarded.

1.2. Integration of diamond defects

To be able to utilize diamond defects in these aforementioned applications, the fabrication has to be done in such a way that does not deteriorate the performance of the diamond color centers. This section discusses diamond integration methods and the challenges associated with that.

Fabrication processes can be categorized into 3 main categories, namely, monolithic integration, heterogeneous integration and hybrid integration. Monolithic integration is when different components are fabricated directly on the same substrate, a typical example is CMOS fabrication process. Heteroge-

neous integration is when two substrates with different materials are integrated together such as wafer bonding, drop casting and spin coating. Finally, hybrid integration is when components are fabricated separately and then integrated on the chip such as pick and place. Drop casting in some cases can be also considered as hybrid integration, namely, this is when the quantum emitters are mixed in a liquid solution and then deposited on the substrate or the chip [29].

A good fabrication process is characterized by high yield and high scalability. Figure 1.4 illustrates these properties for different integration methods. Note that the figure illustrates the integration methods of different quantum emitters, such as quantum dots, and it is not restricted to diamond color center only. Nevertheless, this still can be used to gain insight in the integration methods that exist and make a qualitative comparison.

Monolithic integration offers the scalability of wafer-scale fabrication, however, the performance of the fabricated diamond chip is not guaranteed. This is due to the hardness of the diamond which requires unconventional processing. the work reported in [30] demonstrates a process developed for diamond cavities on SiO_2. While the process results showed good agreement with the simulations, the performance limiting factor was the purity of the diamond itself, which present another challenge in growing pure diamond.

As for heterogeneous integration, wafer bonding has been considered for diamond on insulator (DOI) wafers. The main challenge with DOI wafer bonding is the chemical stability of diamond, which tends not to create bonds with other materials in normal conditions. This requires special treatments to facilitate diamond bonding with the insulator material [31, 32]. In addition, smooth surface on the insulator material is required for direct bonding, which can be challenging to achieve. While wafer-bonding does offer some scalability, however, the yield is still dependent on the treatment that is needed for the bonding.

Alternatively, hybrid integration can be done using pick and place. The main advantage is the high yield it offers when compared to other integration methods. This is mainly because pick and place does not require chemical processing or diamond-on-insulator bonding which has minimal affect on the optical performance hence the high yield. In addition, pick and place is not limited by the material of the receptor chip which makes it very convenient for research applications where nanofabrication methods are not necessarily accessible. Large scale integration is limited, due to the lack of automation techniques of pick and place. Therefore, automating pick and place can help increase the scalability of the process and thus make it feasible for commercial applications.

In practice, integration methods are combined to get the best out of each method [29]. For diamonds, a more realistic integration scheme is when the diamond chip is fabricated monolithically and then integrated in the receptor chip using either wafer-bonding or pick and place [31]. This integration scheme is discussed in the next section.

1.2.1. 3D integration

System level integration requires the compact integration of not only the diamond defects, but also all the components that are needed for control and read out. One way to do that is 3D integration as proposed here [31]. This is illustrated in fig. 1.5, where the aim is to integrate the diamond color centers in a photonic integrated chip with other optical components such as SNSPDs, beam-splitters and MEMS optical switches to excite the color center and detect fluorescence [31]. In addition, a magnetic filed generator is needed to bias and drive the spin state in the diamond. Finally, a cryo-CMOS chip is needed to control the drive and detect the electrical signal coming from the SNSPD. The cryo-CMOS chip is integrated in a flip-chip manner via an interposer containing the micro-bumps as illustrated in fig. 1.5.

This integration scheme allows for efficient use of chip area. However, the challenge lies in the fabrication process as it requires monolithic fabrication process, which is challenging given the materials of the components that are to be integrated, such as diamond and niobium titanium nitride (NbTiN) to name a few [31].

1.2.2. Pick and place for SiN photonics

Previous work has been done in pick and place integration of diamond chiplets [33], however, this work was done on an aluminium nitride (AlN) photonic chip. AlN photonics offer interesting properties such as high electro-optic coefficient which makes them suitable for electro-optical devices such as phase shifter [34], high thermal conductivity, which makes them tolerate high optical powers [35], and high

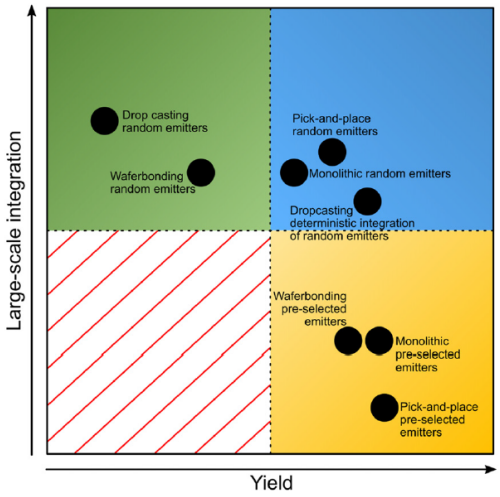

Figure 1.4: Comparison between different quantum emitter integration methods [29]. Note this comparison is not restricted to diamond based quantum emitters, however, it does provide an overview of the relevant integration methods.

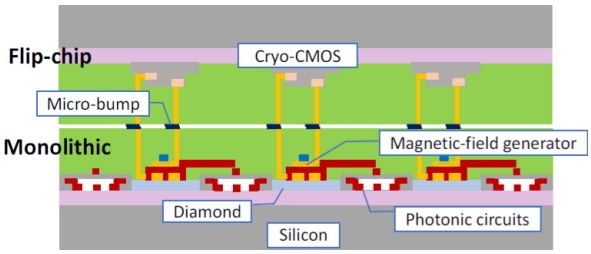

Figure 1.5: an artist impression of the 3D integration scheme of diamond based quantum processor [31].

piezoelectricity which makes them suitable for strain tuning of color centers [36]. However, they suffer from higher propagation losses which is $0.42 dB/cm$ at telecom wavelength [37], whereas the propagation losses of SiN is $0.157 dB/cm$ at the same wavelength [38]. Note that these values indicate the potential propagation losses and not necessarily the real propagation loss achieve, as propagation losses highly depend on the fabrication process, which will be shown later in section 2.1.2. Nevertheless, the literature suggests that propagation losses can be further reduced by using SiN photonics which is prioritized in this project.

1.3. Problem statement and objective

This project is a part of 3D integration project as proposed in [31] and illustrated in fig. 1.5. The focus of this project is to integrate the diamond chip containing the color center in a SiN photonic chip using pick and place assembly. The diamond chip of interest is shown in fig. 1.6 with center of the crossing containing the SnV color center. The color center is exited by $515nm$ light source via one path and then the fluorescence at $620nm$ is collected via the other path.

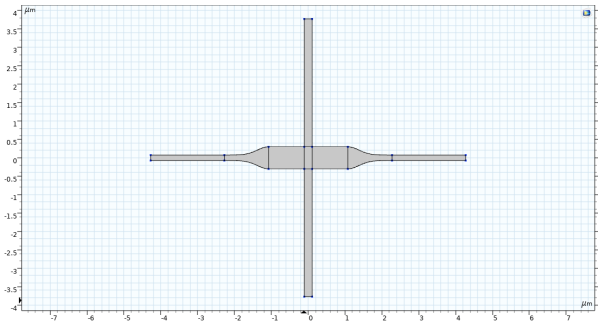

Figure 1.6: Diamond chiplet to be integrated in SiN photonic chip using pick and place.

In order to successfully integrate the diamond chip, the following components have to be designed:

1. Diamond waveguide to SiN waveguide coupler.
2. Mechanical support structure which protects the chip from damage during the pick and place process while keeping the added losses minimal.

Each of these components must satisfy the following requirements:

- Optical coupler:
  1. The coupling efficiency must be $\geq 90\%$. This requirement ensures that the light is coupled to the fundamental mode of the waveguide.
  2. The transmission must not be lower that 90% which translates to insertion loss of $< 0.5dB$. This is to ensure that some power will survive the losses in the subsequent components and thus be able to perform power measurements at the output.
  3. The 3dB misalignment tolerance must be at least $50nm$. This requirement determines the candidate chiplets for further optical measurement. If the integrated chiplet shows higher misalignment than that of 3dB misalignment, then optical measurements is futile.
  4. Footprint must be as low as possible.
- Mechanical support structure:
  1. The added losses by the support structure must not exceed 10%.
  2. The cross talk must be lower than 10%.
  3. Footprint must be as low as possible.

The goal is therefore to find an optimum optical coupler design that meets the requirement with minimal footprint and optimize the support structure for mechanical robustness, minimal footprint and minimal added optical losses. Once these designs are fabricated, pick and place assembly is to be performed followed by transmission measurements to determine the yield.

1.4. Thesis synopsis

This thesis is divided as follows. First, in chapter 2 the theory is underlined by describing the main mechanisms understanding where they come from and relate them to the simulations. Then, chapter 3 dives into the design process and the various simulations that have been performed to optimize the design. After that, the pick and place process is described, including the equipment that have been used and the test plan to determine the yield of the process. That is followed by chapter 4 where the results are presented with discussion on observations that have been made during the process. Finally, chapter 6 draws the main conclusions of this project followed by chapter 6 discussing future recommendation.

2

Theory of Photonics Devices

2.1. Single mode optical waveguides

The purpose is to design a certain physical medium in which the light can propagate over distance in the photonic integrated chip. Ideally, such medium has to be homogeneous, linear, non-dispersive, lossless and isotropic. This section discuss guiding light in waveguide structures.
A propagating electromagnetic wave is described by its electric field and magnetic field components as follows:

$$\mathbf{E}(\mathbf{r},t) = \mathbf{E^0}(x,y)\exp i(kz \pm \omega t) \tag{2.1}$$

$$\mathbf{H}(\mathbf{r},t) = \mathbf{H^0}(x,y)\exp i(kz \pm \omega t)$$

where ω is the angular frequency. The term kz indicates that the light is propagating along the z direction with k propagation constant which indicates the change of the phase in space, in this case, z direction, i.e. $\frac{\partial\phi}{\partial z} = k$. The propagation constant is inversely related to the wavelength $k = \frac{2\pi}{\lambda} = n\frac{2\pi}{\lambda_0}$ with n being the refractive index defined by the material of the medium , and λ_0 is the free space wavelength. This relation can be also expressed as $k = nk_0$ which intuitively suggests that the refractive index is a measure of how much the propagation constant increases for a certain material with respect to the free space propagation constant.

2.1.1. Slab waveguide

The slab waveguide is the simplest form of a waveguide which can be solved analytically. The core is a dielectric material layered between two insulating materials. The main principle is having light ray E_i incident at an angle θ_1 with respect to the core of the slab waveguide called the angle of incidence. A fraction of the light is reflected in the slab core, denoted as E_r, and another fraction is transmitted into the cladding. This reflection satisfies Snell's law

$$n_1 sin(\theta_1) = n_2 sin(\theta_2) \tag{2.2}$$

where n_1 is the refractive index of the core, n_2 is the refractive index of the cladding and θ_2 is the angle of reflection. The relation between the incident light and the reflected light is $E_r = RE_i$ where R is the reflection coefficient as expressed by the Fresnel equation.

$$R_{TE} = \frac{n_1 cos(\theta_1) - n_2 cos(\theta_2)}{n_1 cos(\theta_1) + n_2 cos(\theta_2)} \tag{2.3}$$

$$R_{TM} = \frac{n_2 cos(\theta_1) - n_1 cos(\theta_2)}{n_2 cos(\theta_1) + n_1 cos(\theta_2)} \tag{2.4}$$

To be able to guide the light in the waveguide core, the incident light has to be fully reflected to the other side of the core, which will then reflect again, and so on as shown in fig. 2.1. Therefore, the light is fully guided in the waveguide core when total internal reflection is achieved, which occurs at

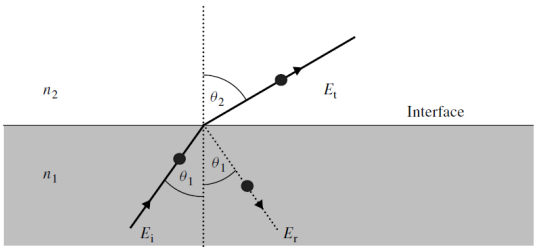

Figure 2.1: Illustration of the light propagation in a 2 planar waveguide. Taken from [39].

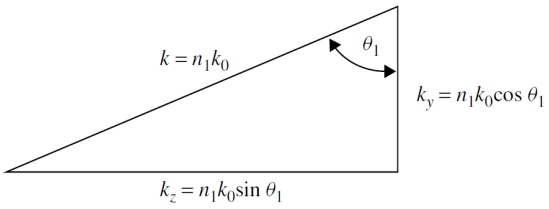

Figure 2.2: Decomposition of the propagation constant in y and z directions. Taken from [39].

$\theta_2 = 90^{circ}$. This can be used to determine the incident angle by plugging $\theta_2 = 90^{circ}$ in Snell's law and re-arranging the formula yields the critical angle

$$\theta_c = sin^{-1}\frac{n_2}{n_1} \tag{2.5}$$

Therefore, the incident angle has to be larger than the critical angle to be able to guide the light in the waveguide core. This can be seen from plugging in Snell's law in Fresnel equations

$$R_{TE} = \frac{n_1 cos(\theta_1) - \sqrt{n_2^2 - n_1^2 sin^2(\theta_1)}}{n_1 cos(\theta_1) + \sqrt{n_2^2 - n_1^2 sin^2(\theta_1)}}$$

$$R_{TM} = \frac{n_2^2 cos(\theta_1) - n_1\sqrt{n_2^2 - n_1^2 sin^2(\theta_1)}}{n_2^2 cos(\theta_1) + n_1\sqrt{n_2^2 - n_1^2 sin^2(\theta_1)}}$$

Substituting eq. (2.5) yields $R = 1$ for both polarizations indicating total internal reflection. If the angle of incidence is lower than the critical angle, then $R < 1$, and if the angle of incidence is higher than the critical angle, then $sin(\theta_1) > \frac{n_2}{n_1}$ which results in a negative square root, i.e. R becomes imaginary, with $|R| = 1$ and with a phase ϕ_r originating from the imaginary part. Therefore, when the angle of incidence is larger than the critical angle, the wave is reflected with an acquired phase. This can be expressed from taking the arctan $\frac{Im(R)}{Re(R)}$ which results in the following

$$\tan\frac{\phi_{r,TE}}{2} = \frac{\sqrt{n_1^2 sin^2(\theta_1) - n_2^2}}{n_1 cos(\theta_1)}$$

$$\tan\frac{\phi_{r,TM}}{2} = \frac{n_1\sqrt{n_1^2 sin^2(\theta_1) - n_2^2}}{n_2^2 cos(\theta_1)}$$

These can be rearranged to the following

$$\phi_{r,TE} = 2\arctan\frac{\sqrt{sin^2(\theta_1) - (\frac{n_2}{n_1})^2}}{cos(\theta_1)} \tag{2.6}$$

$$\phi_{r,TM} = 2\arctan\frac{\sqrt{(\frac{n_1}{n_2})^2 sin^2(\theta_1) - 1}}{(\frac{n_2}{n_1})cos(\theta_1)}$$

Figure 2.2 illustrates the decomposition of the propagation constant at the reflection point for a waveguide core thickness of h where the direction of propagation is in the z direction and the total internal reflection occurs in the y direction. The phase in the y direction can be expressed $\frac{\partial\phi}{\partial z} = k$

$$\frac{\phi_y}{2h} = k_y \rightarrow \phi_y = 2hn_1 k_0 cos(\theta_1) - \phi_{r,upper} - \phi_{r,lower} \tag{2.7}$$

where $2h$ is the total distance the wave travels in the y direction. The phase in the y direction is then composed of the phase of the wave $2hk_y$ and the phase acquired from the reflection with the upper cladding $\phi_{r,upper}$ and the lower cladding $\phi_{r,lower}$. Note that the negative sign is due to the phase being

associated with the reflection of the wave. For a coherent wave propagation, the total phase must be a multiple of 2π. Therefore,

$$2hn_1k_0cos(\theta_1) - \phi_{r,upper} - \phi_{r,lower} = 2\pi m \tag{2.8}$$

where m is an integer. This introduces the notion of propagating modes where the number of mode is set by m. This means that mode m can only propagate when first, $\theta_1 > \theta_c$ and second when θ_1 satisfies eq. (2.8). This means that for a given waveguide core thickness h, the number of guided modes is limited by the first criterion. This is an important realization, since n_1 is fixed by the material, the thickness of the waveguide core is the design parameter to ensure that the waveguide is a single mode waveguide for which $m = 0$.

This can be further understood by substituting eq. (2.6) in eq. (2.8) which yields the following for the TE polarization

$$2hn_1k_0cos(\theta_1) - 2\arctan\frac{\sqrt{sin^2(\theta_1) - (\frac{n_2}{n_1})^2}}{cos(\theta_1)} - 2\arctan\frac{\sqrt{sin^2(\theta_1) - (\frac{n_3}{n_1})^2}}{cos(\theta_1)} = 2\pi m$$

where n_3 is the refractive index of the lower cladding. For a symmetrical waveguide i.e. slab waveguide, $n_3 = n_2$, therefore, this relation for the TE polarization can be reduced to the following

$$\tan\frac{hn_1k_0cos(\theta_1) - m\pi}{2} = \frac{\sqrt{sin^2(\theta_1) - (\frac{n_2}{n_1})^2}}{cos(\theta_1)} \tag{2.9}$$

for TM polarization

$$\tan\frac{hn_1k_0cos(\theta_1) - m\pi}{2} = \frac{\sqrt{(\frac{n_1}{n_2})^2sin^2(\theta_1) - 1}}{(\frac{n_2}{n_1})cos(\theta_1)} \tag{2.10}$$

This can be used to determine the desired number of guided modes given θ_1. For a $\theta_1 \geq \theta_c$, the right hand side becomes zero, and the argument of the tangent should then satisfy $cos(\theta_c) \leq \frac{\pi}{hn_1k_0}$. This expression shows that the maximum limit on the critical angle. Therefore, for a given wavelength, as embedded in k_0, the single mode operation should be determined by choosing the waveguide core material and then choosing the thickness for which the waveguide remains single mode.

In practice, instead of designing in terms of θ_1, it is more convenient to use the effective index of the mode, which is defined as $n_{eff} = n_1sin(\theta_1)$. Plugging that in the critical angle condition eq. (2.5) yields the condition in terms of n_{eff}

$$n_{eff} > n_2 \tag{2.11}$$

For an asymmetrical waveguide, n_2 is set by the lowest refractive index of the two cladding materials. This is the method followed later in section 3.1 to design single mode waveguides. As seen from eq. (2.5), the critical angle is set by the ratio of the refractive index n_2/n_1 which must be lower than 1. Therefore, the refractive index of the core must be larger than that of the cladding.

2.1.2. Loss mechanisms in optical waveguides

So far it has been assumed that light propagates ideally in the material. However, in reality, there are number of reasons that give rise to losses in the waveguide.

In reality, as the light propagates through the medium, the light intensity decays exponentially with the losses associated with the medium. Namely, $E = E_0 \exp -z\alpha$ where α is the loss coefficient. This can be represented as an imaginary effective index that exponentially decays the light intensity. Therefore,

$$\alpha = k_0Im(n_{eff}) \tag{2.12}$$

This propagation loss, typically expressed in dB/cm, consists of many loss mechanisms that are dependent on many factors such as material, wavelength and propagation.

One loss mechanism is absorption loss, where the core material has a light absorption coefficient which induces losses in the intensity as the light propagates through the material. The light absorption coefficient of the material changes with wavelength, therefore, given a certain desired wavelength, the material of the lowest absorption coefficient should be chosen. However, material choice in photonics

might limit the functionality and the performance of photonic devices, as some materials are more suitable for certain photonic devices than others. In some cases, this presents a trade-off between losses and device performance as discussed in section 1.2.2.

Another loss mechanism is the radiation loss. Radiation loss represents higher modes propagating in the cladding of the waveguide, called leaky modes. The thickness of the waveguide determines how many leaky modes are guided in the cladding, therefore, the thickness can be chosen such that no leaky modes can be guided. However, the optimized thickness for the photonic devices are not necessarily in agreement with the thickness for reduced leaky modes. Varying the thickness across the photonic chip adds a significant challenge to the fabrication process which potentially adds more surface roughness and thus more losses. Consequently, it is preferred to fix the thickness across the photonic chip. Therefore, designing the thickness for device performance vs suppressed leaky modes is a trade-off. As the leaky modes propagate through the cladding, they can couple to the Si substrate. To prevent that, a thick SiO_2 layer between the core and the substrate limits this undesired coupling.

Bending loss is a relevant loss mechanism when routing the waveguide in the photonic chip. When bending the waveguide, the arc length of the outer side of the core is longer than the arc length of the inner side. This causes the field at each side of the waveguide core, i.e. the evanescent field, to experience different propagation distance z. However, both evanescent field components need to travel at the same phase, and thus the propagation constant of the outer evanescent field effectively decreases to keep the phase matched with the field in the core. This translates to higher wave velocity, since it is defined as $v = \frac{\omega}{k}$.
This however cannot keep up indefinitely. As the bend increases, the required velocity can increase beyond c which is not physical and thus the evanescent field is lost via radiation.

Finally, fabrication non-idealities, namely, surface roughness of the layers causes scattering of the light as it propagates through the core layer. As the mode is guided in the waveguide by repeated reflection at the surface of the core, high roughness of the surface results in scattering of the light and thus cause lower light intensity with distance as a fraction of it is scattered at each reflection.

2.2. Optical couplers

2.2.1. Coupled mode theory

So far, ray optics has been used to understand guiding modes in slab waveguides. However, the electromagnetism has to be used to understand how 2 modes couple with each other. Suppose we are interested in coupling the modes a and b with their electric field and magnetic field components expressed as follows

$$\mathbf{E_a}(\mathbf{r}) = \mathbf{E_a^0}(x,y)\exp i\beta_a z \tag{2.13}$$

$$\mathbf{H_a}(\mathbf{r}) = \mathbf{H_a^0}(x,y)\exp i\beta_b z$$

The total coupled mode is expressed as an expansion of modes a and b, as follows

$$\mathbf{E_c}(\mathbf{r}) = \mathbf{A}(z)\mathbf{E_a}(\mathbf{r}) + \mathbf{B}(z)\mathbf{E_b}(\mathbf{r}) \tag{2.14}$$

$$\mathbf{H_c}(\mathbf{r}) = \mathbf{A}(z)\mathbf{H_a}(\mathbf{r}) + \mathbf{B}(z)\mathbf{H_b}(\mathbf{r})$$

where the coefficients are functions of z due to the propagation being in the z direction. Intuitively, it is expected of the $A(z)$ and $B(z)$ coefficients to be somehow related to the coupling factor of the modes a and b. This is shown in the coupled mode equation. The coupled mode equation describes the coupling between mode a and b given that the total mode is treated as an expansions. The full derivation of the coupled mode equation can be found here [40]. Here, the purpose is understand how modes couple to each other to be able to do insightful simulations. The equation for coupling mode m to mode n is as follows:

$$\frac{d}{dz}C_m = \sum_m i\kappa_{mn}C_n \exp i(k_n - k_m)z \tag{2.15}$$

where m is an integer and

$$\kappa_{mn} = \frac{\omega\int_{-\infty}^{\infty}\int_{-\infty}^{\infty}(\epsilon_m - \epsilon_n)\mathbf{E_m^0}^* \cdot \mathbf{E_n^0}dxdy}{\int_{-\infty}^{\infty}\int_{-\infty}^{\infty}\mathbf{E_m^0}^* \times \mathbf{H_n^0} + \mathbf{E_n^0} \times \mathbf{H_m^0} \cdot \hat{z}dxdy} \tag{2.16}$$

denotes the coupling coefficient between modes m and n where $\Delta\epsilon = \epsilon_m - \epsilon_n$ and $\mathbf{E_a^{0}}^*$ and $\mathbf{E_b^0}$ are the mode field profiles which is defined by the diameter of the region in which the power is focused up to its $|1/e|^2$ value. This expression suggests that for high coupling efficiency, both fields need to have matching mode field profiles. This explains why fiber to waveguide coupling with high efficiency is challenging, as the mode field profiles are not matched, more specifically, the difference between the spot size of the fields is high. Therefore, spot size converters are used to bring the mode field of the fiber to match the mode field profile of the on-chip waveguide and thus efficiently couple the two modes [41]. Equation (2.15) can be then expanded for A and B as follows:

$$\frac{d}{dz}A = i\kappa_{aa}A + i\kappa_{ab}B\exp i(\beta_b - \beta_a)z \tag{2.17}$$

$$\frac{d}{dz}B = i\kappa_{bb}B + i\kappa_{ba}A\exp i(\beta_a - \beta_b)z$$

where the coefficients can be determined in a similar manner as in eq. (2.16). For a lossless waveguide, $\kappa_{ab} = {\kappa_{ba}}^*$, which can be deduced from eq. (2.16) for κ_{ba}. As for κ_{aa} and κ_{bb}, they are called the self-coupling coefficients which correspond to the propagation constant of the mode. This can be seen from the expression of $A(z)$ and $B(z)$

$$A(z) = \tilde{A}(z)\exp i\kappa_{aa}z = \tilde{A}(z)\exp i\beta_a z$$

$$B(z) = \tilde{B}(z)\exp i\kappa_{bb}z = \tilde{B}(z)\exp i\beta_b z$$

Another observation from eq. (2.17) is the that not only the mode field profiles have to be matched, but also the phases of the modes. For $\beta_b - \beta_a = 0$, then the coupling is maximized by maximizing κ_{ab}, however, if this is not the case, then the additional phase in the exponential weighs the total coupling. Therefore, eq. (2.17) be expressed in terms of $\tilde{A}$ and $\tilde{B}$ as follows

$$\frac{d}{dz}\tilde{A} = i\kappa_{ab}\tilde{B}\exp i\delta\beta z \tag{2.18}$$

$$\frac{d}{dz}\tilde{B} = i\kappa_{ba}\tilde{A}\exp -i\delta\beta z$$

where $\delta\beta = \beta_b - \beta_a$ denoting the phase difference between the modes.

2.2.2. Tapered adiabatic couplers

Adiabatic couplers couple the mode from one waveguide to another by gradually changing one property, such as waveguide width, thickness of the separation between two waveguides. The full derivation is done here [42]. The coupling occurs between the mode in a segment denoted A , and the mode in the subsequent segment denoted B, for which the varying property ρ is changed by a small amount. This is expressed as follows:

$$\frac{d}{dz}\tilde{A} = i\frac{d\rho}{dz}\kappa_{ab}\tilde{A}\exp i\delta\beta z \tag{2.19}$$

Here, the coupling coefficient is weighted by the rate of change of ρ. For adiabatic coupling this should be low, and thus modes couple weakly to each other. $\frac{d\rho}{dz}$ can be designed is such a way that satisfies

$$\zeta = \frac{d\rho}{dz}\frac{\kappa_{ab}}{\delta\beta} \tag{2.20}$$

where ζ is a constant for which $\frac{d\rho}{dz}$ is adiabatic when $\zeta \ll 1$ [42]. For taper couplers, the varying parameter is refractive index in z. The derivation of κ_{ab} for taper couplers has been done here [43]

$$\kappa_{ab} = \sqrt{\frac{\epsilon_0}{\mu_0}}\frac{k_0}{4\delta\beta}\int_A {\mathbf{e_b}}^* \cdot \mathbf{e_a}\frac{\partial n}{\partial z}^2 dxdy \tag{2.21}$$

where $\mathbf{E_m^{0}}^*$ and $\mathbf{E_n^0}$ have been replaced by ${\mathbf{e_b}}^*$ and $\mathbf{e_a}$ denoting the normalized mode field profiles. Equation (2.21) and **??** indicate that when the mode differences between the waveguides is too large, then the taper has to be very long to efficiently couple the modes. This is not only a footprint problem,

but also propagation loss becomes more significant as the taper length increases [44]. Therefore, this makes adiabatic couplers more suitable for coupling modes whose overlap is not too large, such as waveguide-waveguide coupling. As for fiber-waveguide coupling, a typical diameter of an optical fiber core is $5\mu m$ which results in a large mode spot size. Coupling such large spot size to a waveguide will require very long tapers (in the order of $100\mu m$ [41]) at which propagation losses become more prominent.

It is out of the scope to do the full derivation as it has already been done here [43], however, it would be insightful to see how the adiabaticity requirement applies to tapers. For the sake of argument, let us assume that the coupling coefficient can be reduced to the following

$$\kappa_{ab} = \frac{const}{\delta\beta}$$

Plugging this in eq. (2.20)

$$\zeta = \frac{dn}{dz}\frac{const}{\delta\beta^2} \tag{2.22}$$

which should be $\ll 1$ for the adiabaticity criterion. Therefore, rearranging yields

$$\frac{dn}{dz} \ll \frac{\delta\beta^2}{const} \tag{2.23}$$

substituting $\beta_a = k_0 n_{eff,a}$ and $\beta_b = k_0 n_{eff,b}$ yields

$$\frac{dn}{dz} \ll \frac{k_0^2}{const}(n_{eff,b} - n_{eff,a})^2$$

which describes the adiabatic requirement for taperd coupler. More accurately, the relation is

$$\frac{dn}{dz} \ll k_0(n_{eff,b} - n_{eff,a})^2 \tag{2.24}$$

as described in [43] and used in [45] where $n_{eff,a}$ corresponds to the effective index at one segment of the taper and $n_{eff,b}$ is that of the subsequent segment. The closer the segments, the lower the difference is between the effective refractive indices, the more adiabatic. Interestingly, once this criterion is satisfied, increasing the length will not add any measurable improvement. This is demonstrated later in section 3.2.4.

2.3. Thin Film Mechanics

Thin film mechanics is becoming more relevant as the photonic devices are becoming thinner. The mechanical stability of the device becomes more questionable as the thickness to length ratio increases. The structures under consideration experience different types of stress. First, intrinsic stress, which is a residual stress from the fabrication process, consequently, this value highly depends on the fabrication process. Nevertheless, $0.5GPa$ have been reported for intrinsic stress in diamond [46]. In addition to intrinsic stress, the structure also experience thermal stress as the structure is cooled down to cryogenic temperatures. An finally, the structure also experiences external load from the tungsten needle during pick and place.

The consequence of stress on such thin and long structures is that they bend with a certain magnitude, causing the optical properties to deteriorate. This is shown in shown in fig. 2.3 (a) where the Si beams bend as a result of stress [47]. The magnitude of the bending, i.e. the deflection, is shown in fig. 2.3 (b) which is already $200nm$ for $40\mu m$ beam. This presents a challenge which requires some design to relief the stress in the beam.

To understand this, consider a beam with length L being secured at both ends. The stress is defined as the force per area. Once the stress reaches the critical value, the beam will become mechanically unstable. The critical stress depends on the geometry of the structure and the stiffness of the material of the structure. For a structure shown in fig. 2.4, the critical stress is given by

$$\sigma_c = \frac{1}{3}\left(\frac{t}{L}\right)^2 \pi^2 E \tag{2.25}$$

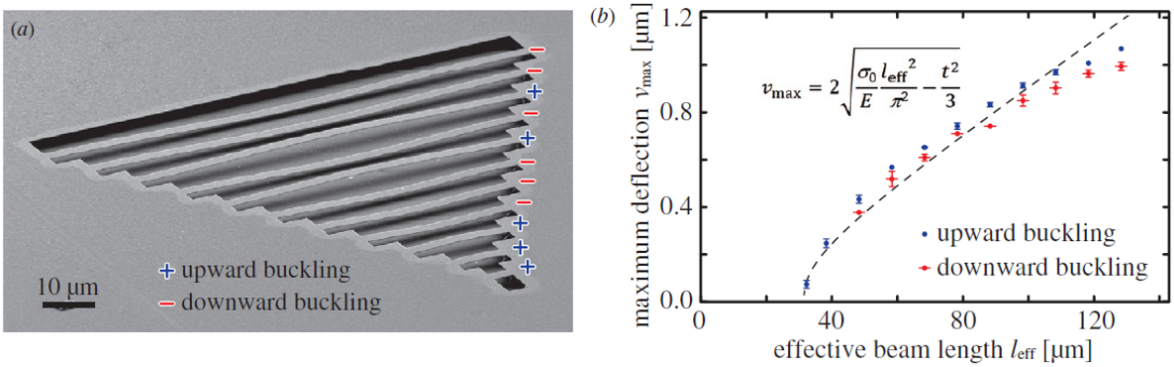

Figure 2.3: (a) Linear buckling in Si beams with $4-100\mu$ lengths. (b) The measured maximum deflection fitted to the calculated maximum deflection as a function of effective beam length. [47].

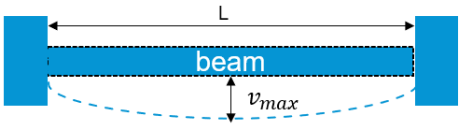

Figure 2.4: Illustration of a beam secured at both ends. Once the beam is subjected to stress, the beam bends with a magnitude corresponding to v_{max} .

where E is the young's modulus indicating the stiffness of the material, and $(\frac{t}{L})$ is the thickness over length ratio. This shows a quadratic dependence of the critical stress on the thickness over length ratio. Therefore, decreasing the thickness causes the structure to become unstable at lower stress values. This requires to decrease the length to keep the critical stress value the same for the lowered thickness.

For a given stress value σ_0, this formula can be rearranged to determine the critical length beyond which the beam becomes unstable

$$L_c = \pi t\sqrt{\frac{E}{3\sigma_0}} \tag{2.26}$$

To put this expressions into perspective, the diamond's Young's modulus is $1050GPa$ whereas the Young's modulus of Si is $169GPa$. Therefore, for a diamond beam of $200nm$ thickness and $40\mu m$ length, the critical stress value is $86MPa$ which is already lower than the intrinsic stress of diamond of $500MPa$ reported here [46]. This means that the length should be decreased to roughly $17\mu m$ to decrease the critical stress value.

As for thermal stress, it is calculated as follows:

$$\sigma = E\alpha\Delta T \tag{2.27}$$

where α is the thermal expansion coefficient, which is $0.610^{-6}K^{-1}$. This stress is equal to $229MPa$ when cooling down the structure to absolute zero, which is also higher than the previously calculated critical stress. This is value is in agreement with the reported thermal stress for diamond which is $215-275MPa$ [46]. Lowering the length to increase the critical stress is not always possible in photonic devices as this will compromise the optical performance, therefore, a supporting structure needs to be designed to release the stress on the beam. For complicated structures, the critical stress expression becomes more complicated which requires advanced simulation tools which can be used for that purpose.

2.4. Waveguide crossings

The importance of considering waveguide crossings in the discussion here is to be able to design a supporting structure for the given diamond chiplet in fig. 1.6. Clearly, the diamond chiplet will make contact with the supporting beam for the beam to provide the required support. Since the support structure is made of the same material as the chiplet, a finite undesired optical coupling will take place between the diamond waveguide and the supporting beam. An easy fix is to reduce the width of the supporting beam and thus reducing the amount of diffraction at the crossing [48]. However, narrow supporting beams might not offer the required support. Therefore, different designs exist to mitigate the diffraction at the crossing without sacrificing the supporting beam with. This section discusses some of these methods.

As the light propagates in the diamond waveguide, the light experiences an abrupt change in the refractive index due to the change in the surrounding material at the crossing point. This requires the angle of incident to accommodate that change for the light to propagate to the other side of the crossing without any losses. However, due to the abrupt change, the incident light cannot accommodate for that thus causing light diffraction [49].

The properties of interest are the insertion loss, defined as Insertion loss is defined as the difference between the input power and the output power in dB.

$$IL = 10\log P_{in} - 10\log P_{out} = -10\log\frac{P_{out}}{P_{in}}[dB] \tag{2.28}$$

and cross-talk, defined as the ratio of the power at an undesired port to the power at the desired port

$$CT = 10\log\frac{P_{port}}{P_{out}}[dB] \tag{2.29}$$

These properties are of interest because they give a measure of how much power is transferred to the output of the crossing and how much power undesirably couples to the other ports with respect to the power at the output. Both, IL and CT, must be as low as possible.

Different designs have emerged to mitigate this problem and thus reduce the losses. Since the cause of scattering is an abrupt change in the refractive index, tapered crossings have been widely researched for waveguide crossings [44, 49, 50]. As discussed in the previous section, adiabatic couplers offer the gradual change in the width of the waveguide such that the propagating mode does not couple to higher order modes and thus prevent losing fraction of the power. Typical insertion loss for these designs is $< 0.5dB$ [50] which already accounts to 10%. These values can be further reduced by considering other techniques, however, often they complicate the fabrication process [44]. The main disadvantage is the large footprint when compared to other designs. For that purpose, Gaussian taper profiles have been used to reduce the area, however, at the expense of lower adiabaticity compared to linear taper profiles [44].

Another design to mitigate this problem is changing the crossing angle where the losses have been minimized at 60^{circ} and 120^{circ}. While this offers accessible fabrication, however, insertion loss is lower than that of tapered crossings [51].

Finally, another method that offers almost unity transmission and simple fabrication is using multi-mode interferometers for which the reported transmission is as high as 99.8%.

2.4.1. Multi mode interferometers (MMI)

The working of MMI is based on the self-imaging principle. The purpose is to guide 2 modes in the MMI such that they interfere with one another as they propagate. Given that the light is excited at the center of the input of the MMI, odd order modes destructively interfere and thus cancel each other due to the symmetry of the device, leaving the even order modes. Therefore, the device width can be chosen such that only the fundamental mode and the second order mode are guided in the MMI.

The propagating mode is therefore a superposition of the two modes propagating at different β. The two modes constructively interfere at certain propagation lengths as shown in fig. 2.5. The interference pattern is then periodically repeated at certain length, hence the name "self-imaging". This length can be determined by first defining beat length

$$L_\pi = \frac{\pi}{\beta_0 - \beta_2} \tag{2.30}$$

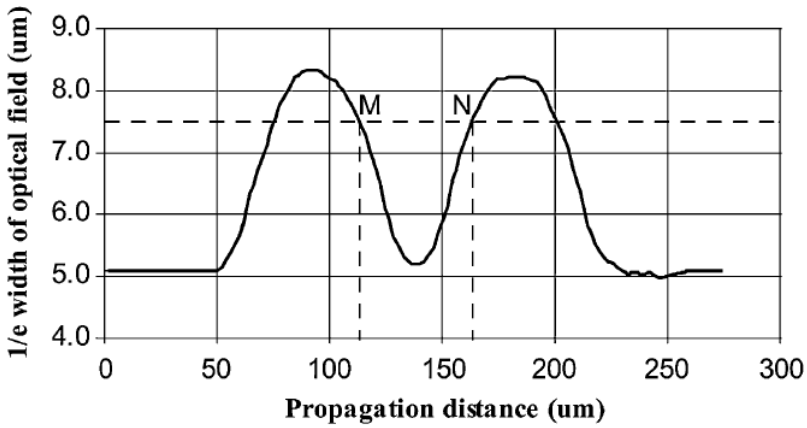

Figure 2.5: The mode field profile of symmetrical MMI as a function of propagation distance simulated using beam propagation method.

which describes the distance between the two modes in the MMI. The interference between the two modes is then repeated at lengths [52]

$$L_{MMI} = \frac{1}{N} 3L_{\pi} \tag{2.31}$$

where N denotes the number of the MMI ports, in this case the MMI is 2×2 and thus $N = 2$. Therefore, $L_{MMI} = 1.5L_{\pi}$. Note that this expression is an approximation, simulations can be done to determines the exact value. Therefore, the self-imaging affect allows to achieve full transmission at the output of the MMI provided the dimensions of the MMI are set properly. In addition, no complicated fabrication process is required for these devices as they can be simply fabricated without any thickness variations. [52–54]

3

Simulation & Design

In order to successfully integrate the donor chip, both the donor and the receptor chip have to be compatible. This section describes the design process and the simulations that have been done to verify the proposed designs. First, the design of the receptor SiN waveguide is described, followed by the design on the donor chip components, namely, the diamond-SiN optical coupler and the mechanical support structure.

3.1. SiN single mode waveguide design

Different waveguide structures which can be used as single mode waveguides for the receptor chip. The strip waveguide (also called ridge or wire waveguide) is chosen due to its simplified fabrication process when compared to the other waveguide structures.
At 620 nm wavelength, the refractive index of SiN is 2.0121 and SiO2 is 1.4574. The refractive index contrast is sufficiently high to allow for light propagation in the waveguide core while minimizing the losses by using SiN as a core material.
The dimensions of the waveguide have to be chosen to ensure that the fundamental mode is the only guided mode in the waveguide core. The width should be also wide enough for full mode confinement in the waveguide core, while simultaneously satisfying the single mode width. As for the thickness, since it is fixed for the whole photonic chip, it should be optimized for the different components that are to be integrated in the same chip.

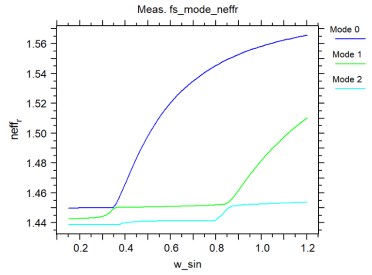

Figure 3.1: n_{eff} of SiN on SiO2 wvaeguide as a function of width at 100 nm thickness.

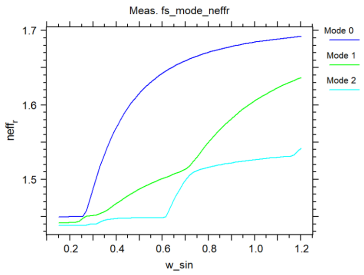

Figure 3.2: n_{eff} of SiN on SiO2 wvaeguide as a function of width at 150 nm thickness.

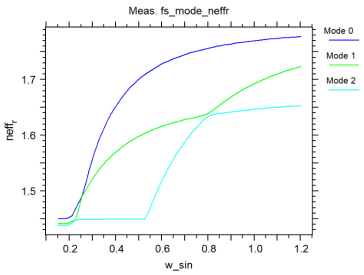

Figure 3.3: n_{eff} of SiN on SiO2 wvaeguide as a function of width at 200 nm thickness.

To determine the right dimensions, mode simulations have been done using the finite element method in RSoft. The simulation results show the effective index of the excited modes as a function of waveguide width at different thicknesses in figs. 3.1 to 3.3. A mode is guided if the effective index of the mode is higher than the refractive index of the cladding, which is in this case $n_{SiO_2} = 1.4574$. Figure 3.1 shows that at 100 nm thickness, the waveguide remains single mode for widths between $400 - 800$ nm. While this width range is sufficiently wide for full mode confinement, however, the optical coupler's losses increase with decreasing thickness. Therefore, a mode simulation has been done for 150 nm (fig. 3.2)

and 200 nm (fig. 3.3) thicknesses. For 150 nm, fig. 3.2 shows the single mode width significantly narrows to 300 nm at which the confinement is deteriorated. As for 200 nm thickness, fig. 3.3 shows that the waveguide is no longer single mode regardless of the width.
The optical coupler is required to couple the light with a minimum transmission of 90 % which is highly prioritized when compared to single mode purity. Consequently, poor confinement also leads to additional losses. Therefore, the chosen thickness is 150 nm and the chosen width is 500 nm. While these dimensions slightly sacrifice single mode purity, they still achieve optimized thickness for different components while minimizing the optical coupler's losses.

3.2. Optical coupler design

3.2.1. Diamond waveguide dimensions

The top diamond waveguide thickness is 200 nm as set by the fabrication process. As for the width, it is set by the design of the diamond cross-waveguide which was not yet determined at the time of conducting this project. Determining this value concretely is out of the scope of this project, therefore the width is set by expecting a reasonable value from the FEM mode simulations shown in fig. 3.4. The results show a single mode width lower than $150nm$ for $200nm$ thickness. This is very narrow which results in poor confinement in the waveguide core which will add more losses in the adiabatic coupler. Therefore, a reasonable width value would be $340nm$ for which the first order mode is also guided. This is not problematic as the first order mode will be filtered out in the adiabatic coupler as will be shown later in section 3.2.4.

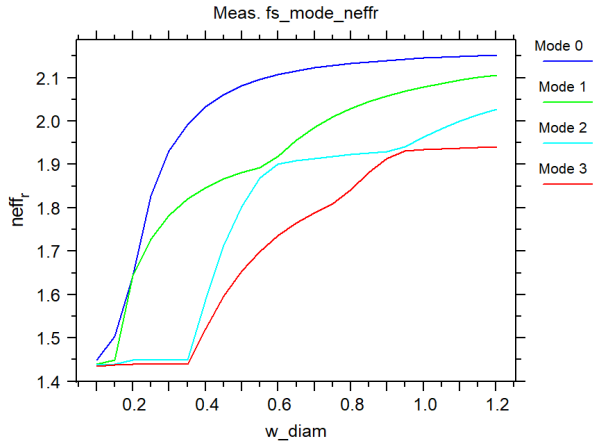

Figure 3.4: FEM simulation of the real part of the effective index for the first 4 modes as a function of waveguide width.

3.2.2. Adiabatic coupler design

Different optical coupler designs can be used for the donor chip. However, the design options are significantly reduced due to the challenging requirement of low optical losses. Therefore, adiabatic couplers are preferred to minimize insertion loss as discussed in section 2.2.2.

The wavelengths of interest are 515 nm for excitation of the SnV and 620 nm which corresponds to the wavelength of the emitted photon. The refractive index of the diamond at these wavelengths is $n_{515nm} = 2.4273$, $n_{620nm} = 2.4114$. The design parameters of the taper are its length and its tip width. The purpose is to have the light coming from the top diamond taper adiabatically couple to the bottom SiN taper as shown in fig. 3.5.

The adiabaticity condition, as stated in eq. (2.24), requires the width of the taper to vary slowly over the length to prevent coupling of the guided mode to higher order modes [55]. Therefore, the taper length has to be sufficiently long to satisfy the adiabaticity condition, but not too long to minimize the footprint and propagation losses.

3.2.3. Adiabatic coupler: taper profile design

Tapered adiabatic couplers come in different geometries as illustrated in fig. 3.6. Each profile requires a certain length to satisfy the adiabaticity requirement. Therefore, it is interesting to see if non-linear taper profiles offer reduced footprint for the same performance. Simulations have been done to compare between the three different taper profiles for SiN waveguide to SiN waveguide coupling. As these simulations are not the main focus of this project, the results can be found in appendix A. Here, linear taper profile is chosen as it exhibits the best performance when compared to non-linear profiles as concluded from the simulations in appendix A.

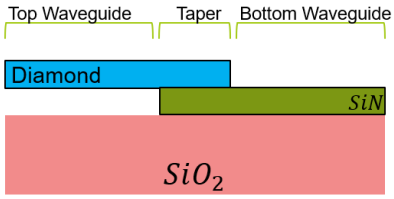

Figure 3.5: An artist impression of the diamond-SiN optical coupler.

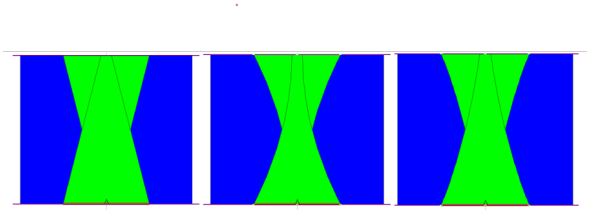

Figure 3.6: Linear, quadratic and exponential taper geometries from left to right.

3.2.4. Adiabatic coupler optimization: linear taper profile

Simulations have been done for different taper lengths and tip widths to determine the optimum dimensions. The simulations were done using the FDTD method due to the taper coupling being out of plane. Figure 3.7 illustrates the total normalized transmission as a function of taper length and taper tip width. The normalized transmission exceeds 90% for taper lengths larger than $6\mu m$ and tip widths up to $100nm$. The maximum transmission is $94,7\%$ occurring at $12\mu m$ length and $40nm$ tip width. Ideally, the tip width should be sufficiently wide to prevent mechanical damage during the pick and place process and to allow for higher misalignment tolerance (as will be shown later).

The maximum transmission for $100nm$ tip width is 92.7% and occurs at $8\mu m$ taper length. These dimensions are much more desirable due to the reduced taper length by 30% and increased tip width by a factor of 2.5 while the transmission being reduced by only 2%. The propagation at these dimensions is shown in fig. 3.9, the insertions loss is 0.32 dB. As for the coupling efficiency, it is simulated by simulating the overlap integral of the output mode with the fundamental mode of the SiN waveguide. The simulated overlap is 92 %, which indicates that the coupled mode is primarily the fundamental mode. The reason why the overlap is not 100 % is because of the design choices of the dimensions of the waveguide. As argued in section 3.1, single mode behavior is slightly compromised for higher confinement and lower losses in the coupler, hence the slightly lower overlap.

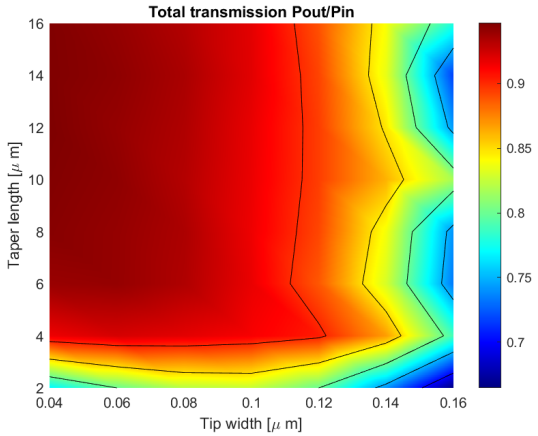

Figure 3.7: FDTD simulation results of total transmission normalized to the input power as a function of taper length and tip width. A $W_{tip}/10 \times 10nm \times 10nm$ mesh is used.

The adiabatic coupler has to work also for the excitation wavelength $\lambda = 515nm$. Therefore, a

FDTD simulation has been done at this wavelength for the propagation from the bottom SiN taper to the top diamond taper. Figure 3.8 shows the propagation profile. The transmission is 93% which translates to insertion loss of $0.3dB$. The coupling efficiency is 91.7%. These values are quite comparable with the collection wavelength which demonstrates the performance of the coupler in the bandwidth range $515 - 620$ nm.

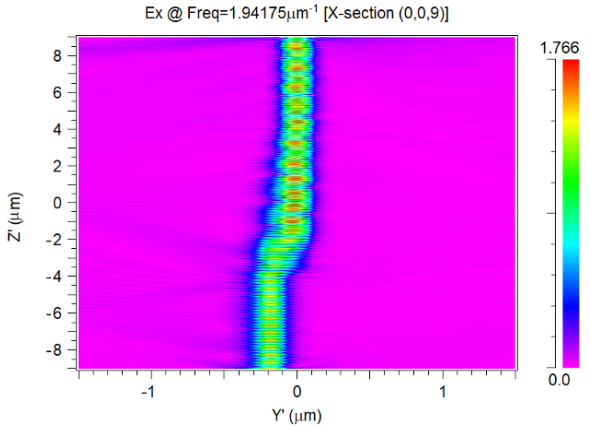

Figure 3.8: X cross section of mode propagation from the bottom SiN taper to the top diamond taper at $\lambda = 515nm$.

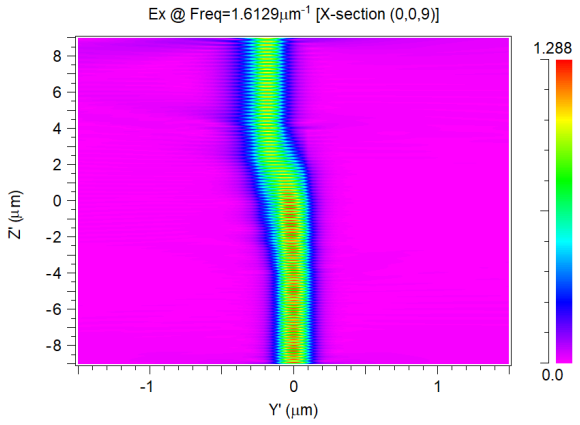

Figure 3.9: X cross section of mode propagation from the top diamond taper to the bottom SiN taper at $\lambda = 620nm$.

The misalignment tolerance is simulated for different misalignment values ranging form $20nm$ to $100nm$. The misalignment in x (z) direction is defined as shifting the top taper in the x (z) direction as shown in fig. 3.10 (fig. 3.11). The results of the FDTD simulation are given in table 3.1 and table 3.2 for misalignment in x and z respectively. Typically, the misalignment tolerance reported in the literature is defined by the 3dB misalignment tolerance at which the transmission is halved. The 3dB misalignment tolerance here is $180nm$ in the x-direction and roughly $5\mu m$ in the z-direction. Since the requirement is to maintain a transmission of minimally 90 %, the misalignment tolerance of interest here is defined as the misalignment at which the transmission satisfies => 90%. Therefore, the maximum misalignment for which the transmission is dropped to 90 % is $800nm$ in the z-direction and $20nm$ in the x-direction. This is rather challenging to achieve in practice without utilizing self-alignment techniques.

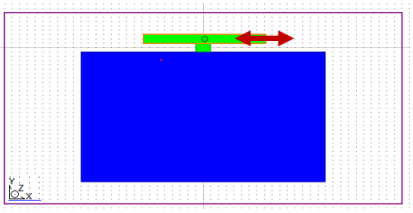

Figure 3.10: Implementation of the misalignment in x direction.

Figure 3.11: Implementation of the misalignment in z direction.

X-Misalignment	Transmission
20 nm	0.9018
60 nm	0.7381
100 nm	0.5863
140 nm	0.5517
180 nm	0.4889

Table 3.1: The simulated transmission at the given misalignment in the x-direction. A $W_{tip}/10 \times 10nm \times 10nm$ mesh is used.

Z-Misalignment	Transmission
0.5 μm	0.958
1 μm	0.862
2 μm	0.856
3.5 μm	0.841
4 μm	0.8
6 μm	0.08

Table 3.2: The FDTD simulated transmission at the given misalignment in the z-direction. A $W_{tip}/10 \times 10nm \times 10nm$ mesh is used.

As expected, the total transmission decreases with increasing misalignment.However, for the mis-

alignment in the x direction, the total transmission remains roughly constant in the $100-140nm$ range. Since the tip width is 100 nm, therefore, in this misalignment range, the top taper and the bottom taper are within 40 nm distance of one another. The constant transmission in this range can be therefore attributed to the coupling of the evanescent field of the top taper to the bottom taper. This property allows to extend the 3dB misalignment tolerance with a few tens of nanometers as the tip width increases. However, the transmission decreases as the tip width increases as seen in fig. 3.7. This demonstrates the trade-off between transmission and misalignment tolerance. For future recommendation, it would be interesting to see if a tip width exists for which the transmission and misalignment tolerance are optimized. This is further discussed in section 6.3. As for the misalignment in z-direction, it gradually decreases until it drops abruptly from 0.8 at $4\mu m$ to 0.08 at $6\mu m$. This occurs at roughly half the taper length.

3.3. Mechanical support structure design

The main challenge with the support structure design is the undesired optical coupling between the supporting beam with the waveguide. At some point, the supporting beam intersects with the waveguide, which results in undesired losses at the crossing. The propagating light experience an abrupt change in the waveguide structure at the crossing, which results in an abrupt change in the effective index. This causes diffraction of the light, which results in significant losses [49, 56]. This section addresses this issue and argues for the proposed designs to minimize the optical losses in the support structure.

3.3.1. Supporting beam width and crossing angle design

As discussed in section 2.4, the diffraction at the crossing can be reduced by reducing the width of the supporting beam, however, if the width is very narrow, then the beam will become more prone to stress, thus not providing the desired mechanical support. Another way to reduce the diffraction at the crossing is by setting the crossing angle in such a way that minimizes the coupling between the waveguide and the supporting beam [51]. Here, a combination of both is considered, where an optimized width and rotation angle can be determined.

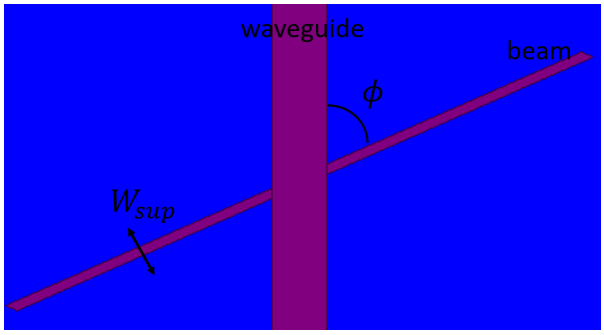

Figure 3.12: The simulated structure indicating the definition of the crossing angle.

An FDTD simulation has been done and the results are shown in fig. 3.13 as a heat-map of the normalized transmission as a function of the crossing angle ϕ and the supporting beam width W_{sup}. The results show and optimum at 60° at which the transmission remains fairly constant. This value is also in agreement with literature [51] where the reported optimized angles were 60° and 120°. The FDTD simulated cross-talk is shown in fig. 3.14 where the lowest cross-talk of $-35dB$ occurs at the same 60° angle.
The results also show that 80° crossing is almost comparable with angled crossing provided the supporting beam width is roughly 100 nm. Therefore, changing the crossing angle helps relaxing the requirement of narrow supporting beam width. However, for this particular project, the maximum achievable transmission is 85% which does not satisfy the requirement. Therefore, another structure is investigated in the following section using multi-mode interferometers.

3.3.2. Multi-mode interferometer (MMI) design

The optical losses at the crossing can be further reduced by using a multi-mode interferometer (MMI) device. As described in section 2.4.1, the MMI can yield a near unity transmission provided the length is

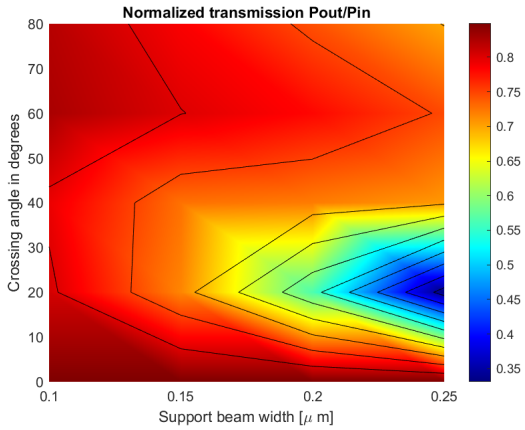

Figure 3.13: FDTD simulated transmission as a function of crossing angle and supporting beam width. A $10 \times 10nm \times 10nm$ mesh is used.

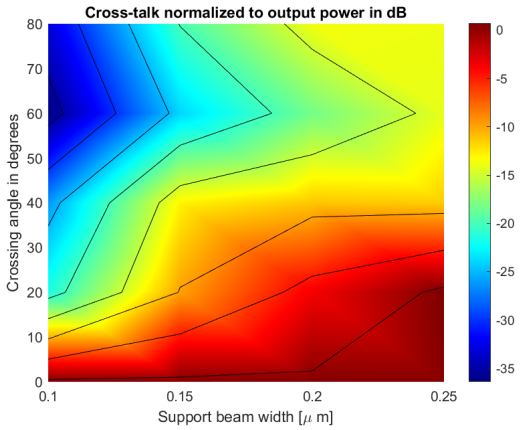

Figure 3.14: FDTD simulated cross talk in dB as a function of crossing angle and supporting beam width. A $10 \times 10nm \times 10nm$ mesh is used.

set properly. The width of the MMI is determined by performing FEM mode simulations as a function of width as shown in fig. 3.4.

The width should be chosen such that both the fundamental mode and the next higher order mode are guided in the waveguide. Since the light is incident on the center of the waveguide, the odd modes cancel out due to the symmetry of the waveguide structure [52]. Therefore, the first higher order mode in this case is the second order TE mode TE_2. For this mode to be guided in the MMI, the width of the MMI should be minimally 550 nm. The length of the MMI is set using **??** as discussed in section 2.4.1 which corresponds to $1.9\mu m$ for $n_{eff_0} - n_{eff_2} = 0.242$ at 550 nm width.

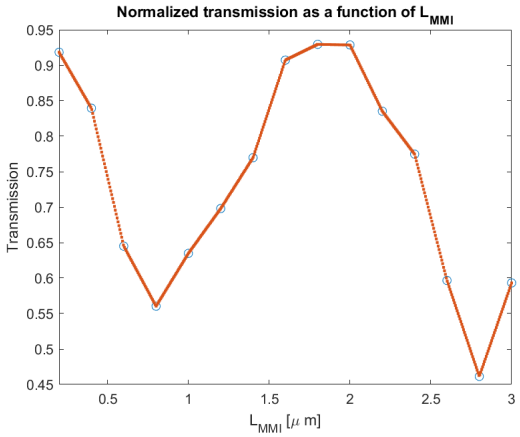

Figure 3.15: FDTD simulation of the normalized transmission as a function of L_{MMI}. A $10 \times 10nm \times 10nm$ mesh is used.

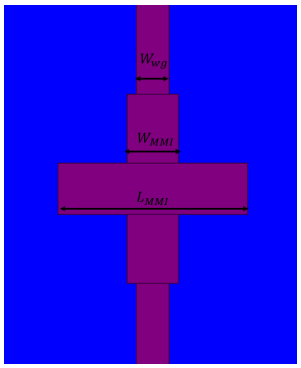

Figure 3.16: Illustration of the simulated structure. The waveguide length is set to $1\mu m$. A $10 \times 10nm \times 10nm$ mesh is used.

Figure 3.15 shows the simulated normalized transmission as a function of L_{MMI}. As expected, the power transfer oscillates with L_{MMI} as the self-images interfere with each other. The simulated MMI length is $2\mu m$ at which the normalized transmission is 94%, which is in agreement with the calculated value $1.9\mu m$. The additional 6% loss can be attributed to scattering at the interface between the single mode waveguide and the MMI. This can be improved by adding a taper between the waveguide and the MMI as demonstrated here [56]. However, this adds additional $2 \times L_{tap} = 16\mu m$ to the total device length for improvement in the transmission with only a few percents. Therefore, the design is kept without taper coupling, which is 10 % improvement over the previous method. As for the simulated cross-talk, it is $-11dB$ as defined in eq. (2.29), which is slightly higher than that of the previous design. Note that the high transmission at $L_{MMI} = 200nm$ should not be confused with self-imaging as the length is too short which can suggest other coupling mechanism such as butt coupling.

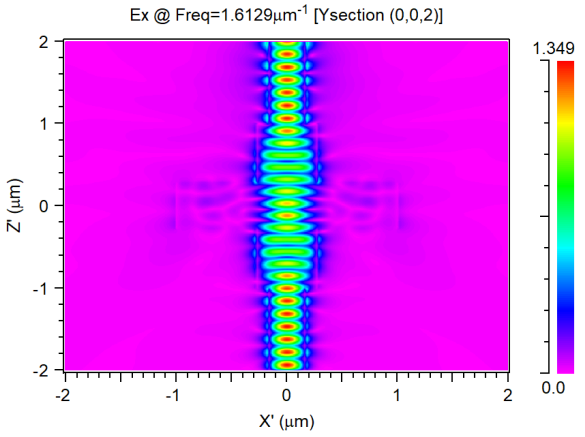

Figure 3.17: Y cross section of the mode propagation in the MMI.

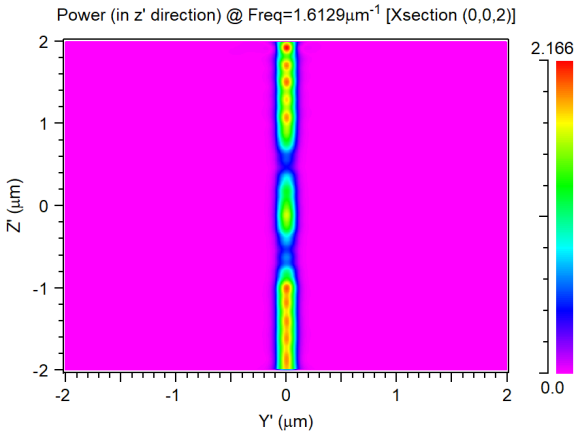

Figure 3.18: Y cross section of the power transfer in the MMI.

Figure 3.17 illustrates the mode propagation through the MMI. This shows the field mode width increasing at the start and then decreasing until the input mode is almost identically replicated at the center. This pattern is repeated again, and the length of the MMI is chosen such that the self-image occurs at the output of the MMI such that it directly couples to the output single mode waveguide. Figure 3.18 illustrates the power transfer, which shows both modes constructively interfering at the center and the output of the MMI. For the x-y section of the field mode profiles at different propagation length, they can be found in appendix B.

3.4. Stress analysis of the donor chip

The resulting donor chiplet design is shown in fig. 3.19. Stress analysis is done to gain insight into the stability of the structure. Ideally, these simulations require knowledge of the boundary loads, which are in this case, the intrinsic load in the diamond, which is the residual stress from the fabrication process, and the load exerted by the tungsten needle on the chip during pick and place process. Both require measurements to be able to acquire these values, however, these measurements are out of the scope of this project. Nevertheless, it is of interest to first examine stress as a result of the structure itself. The boundary load in this case is therefore gravity.

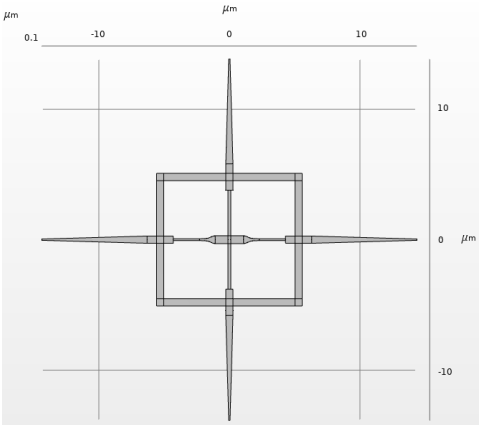

Figure 3.19: The total design of the diamond chiplet including the support structure and the optical couplers.

To perform this simulation, the diamond chiplet is attached to the wafer via 8 tethers from which the chiplet is released to be able to pick up the chiplet during pick and pace. The tethers and the wafer parts are fixed. The stress simulation result is shown in fig. 3.20. The simulated critical stress is

$sigma_c = -8.86GPa$where the negative sign indicates the tensile stress. The critical stress described in eq. (2.25) can be used as a rough approximation to put the simulation results into perspective. Plugging the diamond's young's modulus $1050GPa$ and the thickness to length ratio $(\frac{0.2}{27.55})$ in eq. (2.25) yields $\sigma_c = 182MPa$. The simulated critical load is a factor 48 higher than the calculated critical load for a beam. It is expected to have a higher critical load for diamond chiplet, however, the simulated value is exaggerated. This is attributed to the fact the modeled boundary conditions are unrealistically constraining. In this case, the fixed constraint on the tethers is ideal, however, in reality the tethers bend slightly accommodating for the stress experienced by the chiplet and thus resulting in lower stress. Therefore, more accurate modeling is required to obtain realistic stress values.

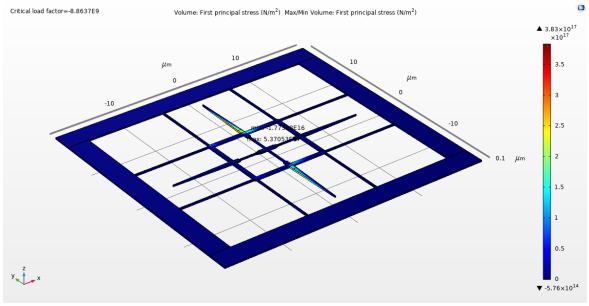

Figure 3.20: The simulated first principal stress in the diamond chiplet.

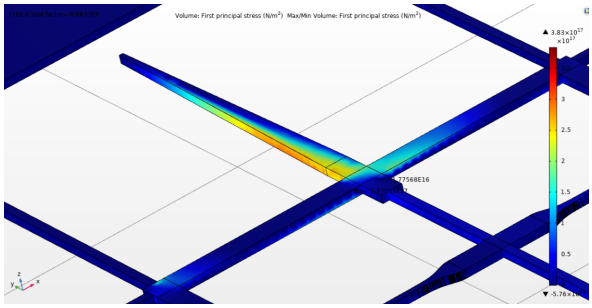

Figure 3.21: The simulated first principal stress in the diamond chiplet zoomed into the part that experiences the highest stress.

4

Pick and Place Integration Process

This chapter describes the equipment that have been used for the pick and place process. In order to reliably perform the pick and place, the equipment must satisfy certain requirements. In addition, a characterization plan is needed to verify the pick and place process. This chapter discusses the main features of the equipment that are used for the pick and place assembly and explains the test-plan to assess the integrated chiplet.

4.1. Pick and place setup

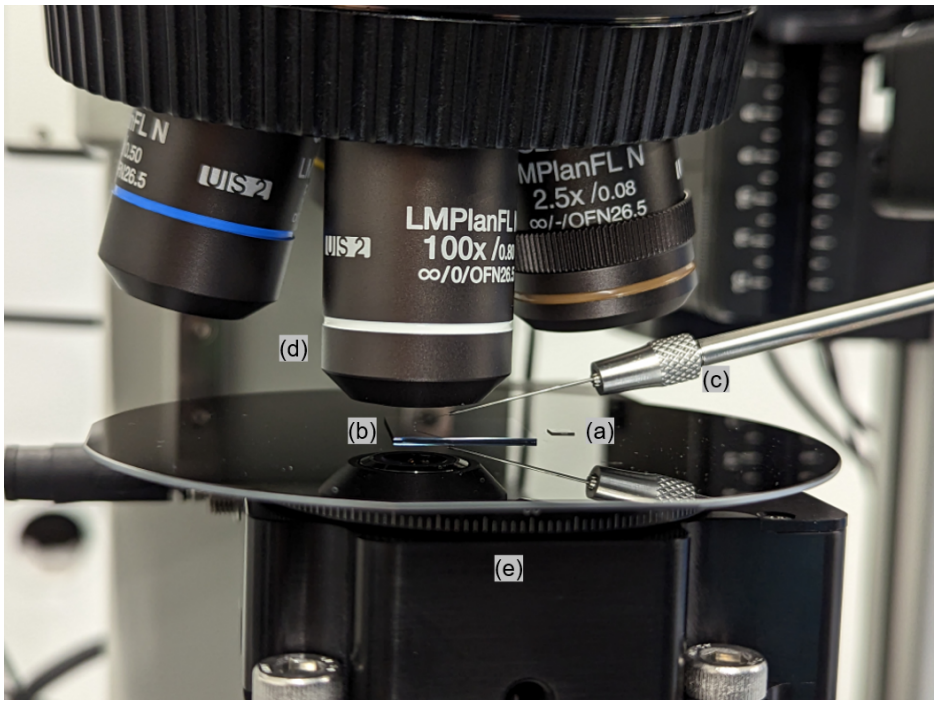

Figure 4.1: A photo of the pick and place setup. (a) is the diamond donor chip containing the diamond chiplets. (b) is the SiN receptor chip. (c) is the tungsten needle with a tip diameter of 200 nm. (d) is 100X objective with 400 nm resolution. (e) is the piezo stage with 47.6 nm step size.

The pick and place setup typically consist of a needle to pick up and place the sample, a piezo stage on which the sample is mounted and finally an objective with sufficient resolution to observe the process. The design of the pick and place setup is done by Alan Yu [1]. This section explains some of

[1]QuTech, Delft University of Technology, Delft, The Netherlands.

the main features of these equipment and argues why these features are satisfying the pick and place requirements. The tota setup is shown in fig. 4.1.

The needle, shown in fig. 4.1 c, needs to be controlled in 3 axes and rotated about the z-axis to be able to conveniently perform the assembly process. Most importantly, since diameter of the needle is in the nano-scale, the material of the needle should be mechanically robust to avoid damage during the process. This makes tungsten needles widely used for pick and place applications as they can be fabricated in a nano-scale and still maintain the required mechanical strength for the assembly process. Tungsten needles are tapered to achieve very thin diameters at the tip. As a rule of thumb, the diameter should be roughly half the size of the supporting beam, therefore, a diameter of 200 nm is chosen using 72X Tungsten Wire (3 mil) Probe 72X-G2/01 from American Probe. The tungsten needle must be placed in a needle holder which is then controlled by a micromanipulator. The micromanipulator needs to have sufficient resolution to perform the manipulations accurately. The used micromanipulator is Eppendorf TransferMan 4r 5193000012.

As for the piezo stage, shown in fig. 4.1 e, needs to be controlled such that the sample can be placed under the objective and aligned with the needle. This requires 3-axes control as well as rotation about the z-axis. The used stage for the x and y axes is ZABER X-LSM100A with $47.6nm$ step size, which is more than sufficient considering the sample size is in the order of tens of microns. As for the rotation control, this is useful to align the receptor chip with the donor chip on the needle. For that purpose, ZABER X-RSW60C-E03 is used.

Finally, the whole process has to be done under the objective, shown in fig. 4.1 d which should have sufficient resolution to be able to align the donor chip with the receptor chip. For that purpose, LMPLFLN100X from Olympus is used with 100x magnification, 0.8 numeric aperture and wavelength range $500 - 600nm$. The resolution can be calculated using $R = 0.61\frac{\lambda}{NA}$ which results in resolution range of $381 - 457nm$. While this resolution is sufficient for picking up the donor chip, it is still not enough to characterize the alignment of the donor with the receptor chip. For that purpose, SEM will be needed to accurately assess the misalignment.

4.2. Pick and place process

The pick and place process is done by first placing the donor and receptor chips on the same wafer. This is done by simply gluing the chips on a Si wafer as shown in fig. 4.1. Then, the needle is brought under the objective using the joystick.

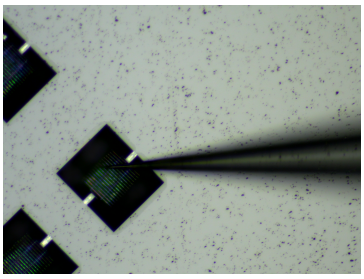

Figure 4.2: Attempt at picking up chiplet $B - 10 - 100$

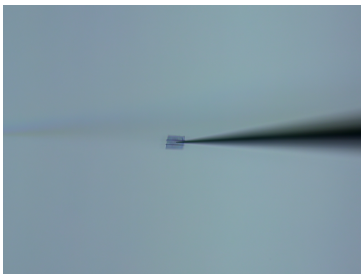

Figure 4.3: Chiplet being picked up by the tungsten needle.

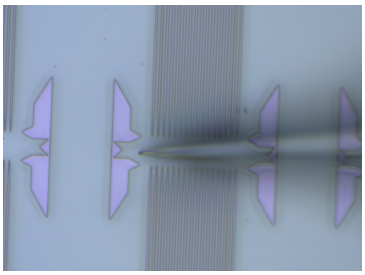

Figure 4.4: Tungsten needle getting in focus as it approaches the receptor chip.

Under the 100X objective, the needle is brought down the z-axis such that it makes contact with the donor chip as shown in fig. 4.2. This can be seen from the needle gradually becoming in focus under the objective. Once the needle tip is fully in focus, then this indicates that the needle is touching the donor chip. By bringing the needle in touch with the donor, van der Waals attraction forces attach the donor chip onto the needle [57]. Then, the needle is lifted up in the z-direction and the chip is successfully picked up with the needle as shown in fig. 4.3.

This is followed by moving the piezo stage to bring the receptor chip under the objective. The receptor chip is then aligned with the donor chip (that is still on the needle) by performing the required rotation of the piezo stage. Once both chips are aligned, the needle is brought down until the donor tapers make contact with the receptor tapers, as shown in fig. 4.4 and thus the donor chip is placed via van der Waals attraction forces with the receptor SiN waveguides.

4.3. Donor chiplets used for the pick and place

While the design has been done for the cross-waveguide chiplet, the donor chiplets that have been used to demonstrate the pick and place process are different due the cross-waveguide not being fabricated at the time of conducting this project. The used donor chip is a diamond chiplet with 16 waveguides of widths ranging from $250nm$ to $340nm$ shown in fig. 4.5, fig. 4.6 and fig. 4.7. The designs are suspended to be able to release them from the chip using the tungsten needle. The pads represent the remaining diamond wafer to which the suspended chiplets are attached. The design and the fabrication of these chiplets have been done by Nina Codreanu [2]. Figure 4.5, fig. 4.6 and **??** show the 3 different support structure designs for each chip. The thickness of these chiplets varies in $400 - 570nm$ range as the fabrication process did not yield unifrom thickness across the chiplet. Each one of these chiplets come in 3 different waveguide lengths, namely, $10\mu m$, $15\mu m$ and $18\mu m$. Stress analysis of these chiplets is given in [**?**].

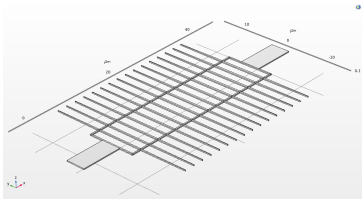

Figure 4.5: Diamond chiplet with bulk attached support structure.

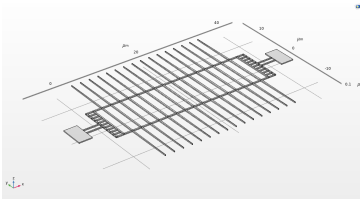

Figure 4.6: Diamond chiplet with double tether attached support structure on both sides.

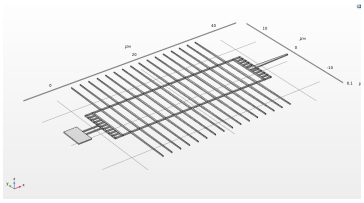

Figure 4.7: Diamond chiplet with double tether attached on one side with a handle on the other side.

Furthermore, the chiplets are fabricated on both 100 orientation and 110 orientation. The purpose originally was to investigate the robustness of the design and the width and thickness uniformity. However, this is also relevant for the pick and place as both robustness and dimension variations play a role in the yield of the pick and place process as will be discussed later in section 5.1.

The main difference between these chiplets and the designed chiplet is the design of the support structure. The width is $250nm$ which is roughly half the width of the support structure design proposed here and the length is $34\mu m$ which is roughly 3 times the length of the support structure of the cross-waveguide chiplet. The similarity lies in the tip width of the tapered adiabatic coupler, however, the tapers of these chiplets are $2\mu m$ longer.

4.4. Receptor chip used for the pick and place

The receptor chip consists of the receptor waveguide to which the diamond waveguide is to be coupled, the fiber to chip optical coupler which will efficiently couple the light to the chip to perform the required measurements, alignment marks to help with aligning the donor chip with the receptor chip and potentially pedestals to support the chiplet once placed [57]. The fabrication of the receptor chip was done by Maurice van der Maas [3].

Due to the fabrication process resulting in high side-wall roughness in the SiN waveguides, propagation losses are too high such that almost all power is lost, and thus no measurement can be done. Therefore, the used receptor chip is fabricated for the purpose of pick and place only, and not for the purpose of performing optical measurements. Therefore, the receptor chip is reduced to SiN receptor waveguides without fiber-chip coupling. Furthermore, to keep the fabrication process as simple as possible, the fabrication of the pedestals has been discarded as it requires additional etching step. Therefore, two receptor chips have been fabricated, one of them containing alignment marks, shown in fig. 4.8, and the other consisting of only SiN waveguides.

4.5. Characterization of the pick and place process

A successful pick and place process is determined by the measured optical transmission. However, the results from this measurement are affected by many factors. The definition of insertion loss takes

[2]QuTech and Kavli Institute of Nanoscience, Delft University of Technology, Delft, The Netherlands.
[3]QuTech, Delft University of Technology, Delft, The Netherlands.)

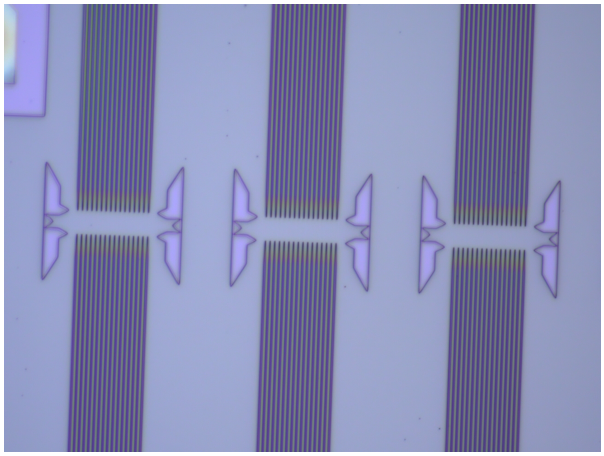

Figure 4.8: Microscope image of the receptor chip showing the tapered SIN waveguides and the alignment marks.

all kinds of losses in the system into account. However, to make meaningful conclusions from the measurements, different loss mechanisms need to be distinguished, to be able to tell by how much each loss mechanism contributes to the total insertion loss. This requires a test plan which aims at isolating the different loss mechanisms.

The total transmission in the receptor chip can be expressed as follows:

$$T_{total} = (T_{SSC} \cdot T_{wg,SiN} \cdot l_{SiN,wg} \cdot T_C \cdot T_{MMI})^2 \cdot T_{wg,diam}$$

where

- T_{SSC} is the normalized transmission of the spot size converter.
- $T_{wg,SiN}$ is the normalized transmission of the SiN waveguide per unit length.
- T_C is the normalized transmission of the adiabatic coupler.
- T_{MMI} is the normalized transmission of the multi-mode interferometer.
- $T_{wg,diam}$ is the normalized transmission of the diamond waveguide.

The squaring corresponds to having 2 of each component in the receptor chip. Ideally, each component has to be characterized separately to be able to determine the losses coming from each component.
First, the transmission of the SiN waveguide has to be measured separately. This is done by simply patterning many waveguides and directly aligning the excitation and collection fibers on both ends of the receptor chip. The optical fiber couples to the waveguide in a butt-coupling manner. Then, the transmission is measured for each waveguide and the mean value is used to determine the average transmission per unit length.
Second, the transmission of the spot size converter has to be measured. The SSC has to be fabricated on both ends of the chip with a waveguide connecting them together to prevent scattering losses. Then the transmission of the SSC can be calculated using $T_{total} = T_{SSC}^2 T_{SiN,wg} l_{SiN,wg}$, therefore,

$$T_{SSC} = \sqrt{\frac{T_{total}}{T_{SiN,wg} \cdot l_{SiN,wg}}}$$

One might consider measuring T_C and T_{MMI} separately, however, this is rather impractical. This measurement will require pick and place of single diamond waveguides which is impractical to align with the receptor waveguide. In this case, the simulation results can be used as indicators to tell how much loss each is adding to the total loss. the simulation results predicts more loss from the adiabatic coupler than from the MMI.

Finally, the alignment can be inspected from SEM images of the integrated chiplets. This will help distinguish between low measured transmission due to component non-idealities or due to misalignment.

The yield is then defined as the number of chiplets that exhibit transmission larger than 90%, are mechanically intact, to the total number of integrated chiplets.

5

Experimental Results of Pick and Place Process

Due to unforeseen circumstances, the fabrication process of the SiN photonic chip did not yield high quality Sin waveguides that can be used for the measurement. This is mainly due to the side-wall roughness that is causing too much propagation losses in the waveguides. Almost 0 transmission was measured, because of the losses being too high. Research is still on going to improve the fabrication recipe such that measurements can be done. However, due to the time constraint of this project, it is decided proceed without these measurement. Nevertheless, a receptor chip has been designed to perform the pick and place though without optical measurements. The results of the pick and place process are discussed in this chapter.

5.1. Alignment results

Figure 5.1, fig. 5.2 and fig. 5.3 show placement attempts of chiplet $B-10-110$ indicating the bulk attached chiplet with $10\mu m$ waveguide length and fabricated on 110 orientation. The figure indicates that the chiplet tolerance for re-attempts is limited. The receptor has been rotated for the needle to approach the receptor chip. This is rather undesirable as it was not possible for the needle to approach the receptor chip at any angle due to the alignment marks having significant thickness of $150nm$. Therefore, another receptor chip has been made.

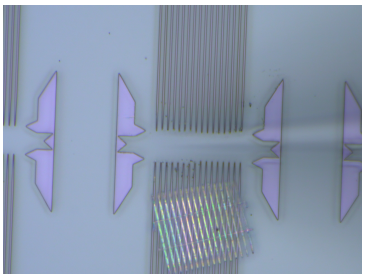

Figure 5.1: Misplacement of chiplet $B-10-110$ fabricated in 110 diamond with waveguide length is $10\mu m$.

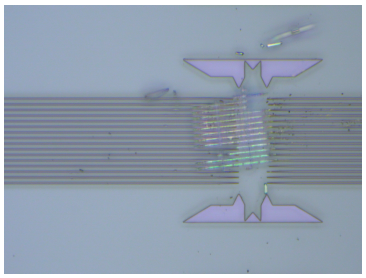

Figure 5.2: Misalignment of chiplet $B-10-110$ fabricated in 110 diamond with waveguide length is $10\mu m$.

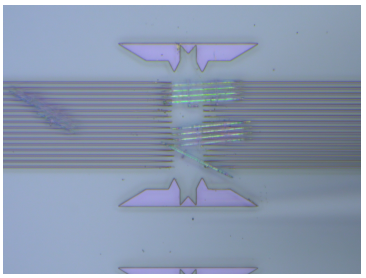

Figure 5.3: Reattempt at aligning chiplet $B-10-110$ fabricated in 110 diamond with waveguide length is $10\mu m$.

The main results of pick and place using the second receptor chip are shown in fig. 5.4 where the results of the first attempt to place the chiplet $H10-100$ is shown. The pick and place of the chiplet was reattempted and the placement is slightly improved as shown in fig. 5.5, however still misaligned. By the forth attempt, the chiplet was disintegrated.

A more successful result is shown in fig. 5.6 with chiplet $B10-100$ having the same waveguide length but different support structure. The placement shown in the figure is the result from the first

attempt. The image still shows roughly $250nm$ misalignment in the x direction and roughly $2\mu m$ in the z-direction. An SEM image will be needed to accurately quantify the misalignment.

These results suggest that the alignment during the placement is rather random. Observations during the placement process have shown that once the chiplet almost makes contact with the receptor, the chiplet quivers in random motion, thus rendering needle alignment almost ineffective. This has been observed in all chiplets regardless of support structure design and crystal orientation.

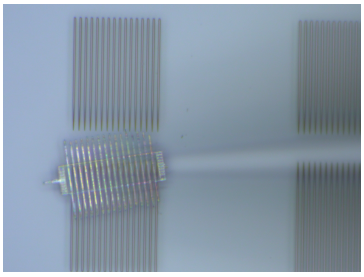

Figure 5.4: Initial placement of chiplet $H10-100$ fabricated in 100 diamond with waveguide length is $10\mu m$.

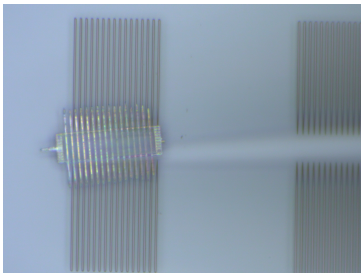

Figure 5.5: Second attempt at placement of chiplet $H10-100$ fabricated in 100 diamond with waveguide length is $10\mu m$.

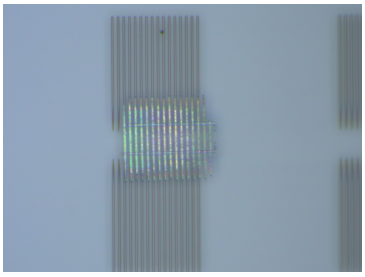

Figure 5.6: Successful placement of chiplet $B10-100$ fabricated in 100 diamond with waveguide length is $10\mu m$.

In addition, abrupt random movement of the chiplet has been also observed, where the chiplet was randomly placed $\approx 50\mu m$ away from the needle shown in fig. 5.7.

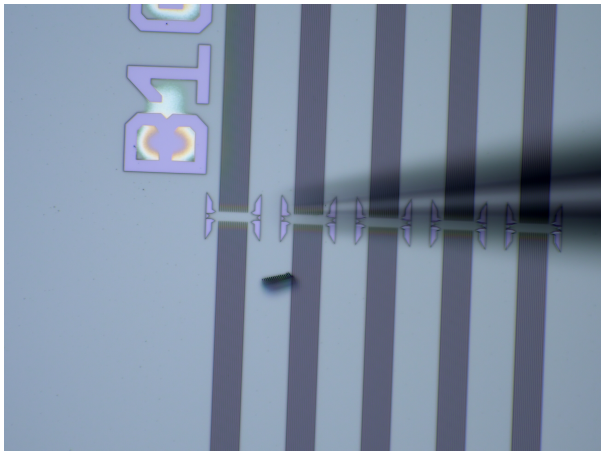

Figure 5.7: Abrupt placement of the diamond chiplet far from the place at which the needle originally was positioned.

Ideally, the yield of the process must be determined by optically measuring the transmission as described in section 4.5. However, since this was not possible, a rough estimate of the yield can be then determined by inspection of microscope images. In total, pick and place has been done on 4 chiplets, one of which is integrated as shown in fig. 5.6 which results in 25% yield. As for the throughput of the process, it is defined as the time it takes for the whole pick and place process per sample, which is 45 minutes per sample.

6

Conclusion & Future Recommendation

6.1. Conclusion

The purpose of this project is to demonstrate pick and place integration of the diamond cross-waveguide chiplet in SiN photonic chip using pick and place. For that purpose, simulations have been done to design optical coupler. A taper adiabatic coupler with linear profile has been optimized at $8\mu m$ length and $100nm$ tip width at which $IL = 0.32dB$ which satisfies the requirement. In addition, the optical coupling between the diamond waveguide and the supporting beam has been investigated for which two designs have been compared. The MMI design satisfies the requirement with $0.27dB$ insertion loss and $-11dB$ cross-talk. Pick and place process has been carried out with diamond chiplets with 50 nm misalignment tolerance and an initial yield estimate of 25%. Transmission measurements were not possible due to the poor performance of SiN receptor waveguides. Nevertheless, 50 nm misalignment is expected to reduce the transmission below 90% which no longer satisfies the requirement. The high misalignment is attributed to the random motion during the placement process originating from surface roughness on both the receptor chip and the lower surface of the diamond chiplet.

6.2. Discussion

The results of the pick and place process suggest that aligning the needle with the receptor chip is rather ineffective as the donor chip makes slight random movements once it is in the vicinity of the receptor chip. One explanation attributes this random motion to the varying thickness of both donor chiplet and receptor chip. As reported, the thickness of the supporting beam in the donor chiplet varies in the $400 - 500nm$ range. This is already large enough to significantly affect the magnitude of the van der Waals attraction forces. Therefore, one part of the chiplet is subjected to higher van der Waals force than another, thus causing the chiplet to slightly move in the direction of the highest attraction forces. Higher thickness uniformity in donor chiplet and lower surface roughness of receptor chip is needed to to be able to reduce the magnitude of this random motion.
In addition, abrupt random movement of the chiplet has been also observed. A movement in such large magnitude is attributed to residual charges in the donor and receptor chip attributed to the fabrication process and SEM previous imaging. This causes the chiplet to move randomly as a result of Coulomb forces between the donor and receptor chips.

While performance of the adiabatic coupler and the MMI have been simulated with satisfying performance, however, in reality it is expected for the transmission to deteriorate for many reasons. First, in these simulations, it has been assumed that the fabrication process is ideal and thus resulting in smooth surfaces. However, in reality, surface roughness can be significantly large in such a way that deteriorates the total transmission. The second reason is that the simulations assume a perfect material without any defects or deformations. In reality, this is not the case as these defects either occur naturally or as a result of invasive fabrication process which can affect how light propagates through the material and thus causing dispersion which leads to the transmission power being distributed among many neighboring wavelengths.

The yield has been estimated to be 25%, however, it is expected that this estimation is rather optimistic. For the aforementioned simulation limitations, it is expected that the measured performance is lower than simulated. As for the support structure, the proposed design is double the width of the used support structure which makes it more robust thus permitting more re-attempts. However, the limiting factor is the random motion as it prevents accurate alignment.

This presents a challenge in alignment during the placement process as misalignment is more dominated by random motion in the vicinity of the receptor chip, more so than the alignment of the needle with the receptor. This requires more research in self-aligning methods and whether or not they can be applied to thin nano-structures.

6.3. Future recommendation

To address the issue of the random motion during the placement of the donor chip, the thickness uniformity of the donor chiplet and the surface roughness of the receptor chip need to be improved. For the donor chiplet, it has been reported that the variation in thickness is more prominent in the lower surface of the chiplet than the upper surface, as a consequence of etching below the chiplet to make the suspended structures. Therefore, placing the chiplet on its top surface can help reduce the magnitude of the random motion by eliminating the lower thickness uniformity on the bottom side and thus improve alignment. For the same purpose, the surface roughness of the receptor chip has to be improved to damp the random motion. Depositing a thin layer of HMDS has been known to decrease surface roughness provided that the deposition rate is properly set [58]. Therefore, treating the receptor chip with HMDS can help mitigate the magnitude of the random motion. As for the random motion caused by Coulomb forces, neutralizing the donor and receptor chip will help limit these forces. This can be done by simply using a de-ionizer.

In addition, alignment can be increased by design such that the random motion is less significant when compared to the dimensions of the optical coupler, namely the tip width. In the design presented here, the increase in the tip width has been limited by the transmission as higher tip widths result in lower transmission. Lower tip widths result in lower misalignment tolerance, and thus lower transmission. Therefore, it would be interesting to investigate whether a tip width exists for which the transmission and the misalignment tolerance are optimized. This requires a simulation of the transmission as a function of the tip width and misalignment. This determines then the value of the highest misalignment tolerance for each tip width at which the transmission is no lower than 90 %. The expected result should show an increasing misalignment tolerance with increasing tip width. Then, this result can be compared with the transmission for each tip width at zero misalignment, which decreases with increasing tip width as seen in fig. 3.7. The results can be plotted on the same graph with one y-axis being the transmission at 0 misalignment, the other y-axis being the misalignment tolerance and the x-axis being the tip width. This can yield insightful results as to how to select the tip width such that it is large enough when compared to the magnitude of the random motion.

Finally, in this work, the successful integration of the diamond chiplet has been characterized by simply coupling power to and from the chiplet. However, the purpose is to have reliable propagation of single photons through the integrated diamond chiplet to the receptor SNSPD. Therefore, it has to be demonstrated that the proposed designs do not deteriorate this property [59]. For that purpose, measurements of the second order correlation function $g^2(\tau)$ have to be performed to rigorously determine the success of the pick and place process and thus the yield.

Acknowledgement

First, I would like to thank Alan Yu for doing a great job with designing the pick and place setup. As pick and place can be a very tedious process, Alan has certainly made it more manageable by choosing the right equipment with features, such as low step size and high objective resolution, which has made the whole process much more easier.

I would also like to thank Salahuddin Nur for the interesting discussions and the helpful guidance in this project. Salahuddin has been always available to answer my questions and suggesting interesting papers which has been very helpful.

I also would like to express my gratitude to Nina Codreanu who designed and fabricated the test-diamond chiplets which have been used to demonstrate pick and place.

I am also thankful to Maurice van der Maas for fabricating the receptor chip and delivering even at short time notice. He also worked on the characterization of the SiN receptor waveguides for which I am also thankful.

I gratefully acknowledge support from the joint research program "Modular quantum computers" by Fujitsu Limited and Delft University of Technology, co-funded by the Netherlands Enterprise Agency under project number PPS2007.

Finally, I also acknowledge DelftBlue for using the supercomputer to perform the FDTD simulations.

Bibliography

[1] Lilian Childress and Ronald Hanson. Diamond nv centers for quantum computing and quantum networks. MRS Bulletin, 38(2):134–138, Feb 2013.

[2] Lucio Robledo, Lilian Childress, Hannes Bernien, Bas Hensen, Paul FA Alkemade, and Ronald Hanson. High-fidelity projective read-out of a solid-state spin quantum register. Nature, 477(7366):574–578, 2011.

[3] Dominik Rohner, Lucas Thiel, Benedikt Müller, Mark Kasperczyk, Reinhold Kleiner, Dieter Koelle, and Patrick Maletinsky. Real-space probing of the local magnetic response of thin-film superconductors using single spin magnetometry. Sensors, 18:3790, 11 2018.

[4] A. Jarmola, V. M. Acosta, K. Jensen, S. Chemerisov, and D. Budker. Temperature- and magnetic-field-dependent longitudinal spin relaxation in nitrogen-vacancy ensembles in diamond. Phys. Rev. Lett., 108:197601, May 2012.

[5] Hong-Quan Zhao, Masazumi Fujiwara, and Shigeki Takeuchi. Effect of substrates on the temperature dependence of fluorescence spectra of nitrogen vacancy centers in diamond nanocrystals. Japanese Journal of Applied Physics, 51:090110, aug 2012.

[6] Luojun Du, Tawfique Hasan, Andres Castellanos-Gomez, Gui-Bin Liu, Yugui Yao, Chun Ning Lau, and Zhipei Sun. Engineering symmetry breaking in 2d layered materials. Nature Reviews Physics, 3(3):193–206, 2021.

[7] Christian Hepp. Electronic structure of the silicon vacancy color center in diamond, 2014.

[8] Matthew E. Trusheim, Benjamin Pingault, Noel H. Wan, Mustafa Gündoğan, Lorenzo De Santis, Romain Debroux, Dorian Gangloff, Carola Purser, Kevin C. Chen, Michael Walsh, Joshua J. Rose, Jonas N. Becker, Benjamin Lienhard, Eric Bersin, Ioannis Paradeisanos, Gang Wang, Dominika Lyzwa, Alejandro R-P. Montblanch, Girish Malladi, Hassaram Bakhru, Andrea C. Ferrari, Ian A. Walmsley, Mete Atatüre, and Dirk Englund. Transform-limited photons from a coherent tin-vacancy spin in diamond. Phys. Rev. Lett., 124:023602, Jan 2020.

[9] Elke Neu, Martin Fischer, Stefan Gsell, Matthias Schreck, and Christoph Becher. Fluorescence and polarization spectroscopy of single silicon vacancy centers in heteroepitaxial nanodiamonds on iridium. Phys. Rev. B, 84:205211, Nov 2011.

[10] Yuri N. Palyanov, Igor N. Kupriyanov, Yuri M. Borzdov, and Nikolay V. Surovtsev. Germanium: a new catalyst for diamond synthesis and a new optically active impurity in diamond. Scientific Reports, 5(1):14789, Oct 2015.

[11] Takayuki Iwasaki, Yoshiyuki Miyamoto, Takashi Taniguchi, Petr Siyushev, Mathias H. Metsch, Fedor Jelezko, and Mutsuko Hatano. Tin-vacancy quantum emitters in diamond. Phys. Rev. Lett., 119:253601, Dec 2017.

[12] Srujan Meesala, Young-Ik Sohn, Benjamin Pingault, Linbo Shao, Haig A. Atikian, Jeffrey Holzgrafe, Mustafa Gündoğan, Camille Stavrakas, Alp Sipahigil, Cleaven Chia, Ruffin Evans, Michael J. Burek, Mian Zhang, Lue Wu, Jose L. Pacheco, John Abraham, Edward Bielejec, Mikhail D. Lukin, Mete Atatüre, and Marko Lončar. Strain engineering of the silicon-vacancy center in diamond. Phys. Rev. B, 97:205444, May 2018.

[13] Peng Wang, Takashi Taniguchi, Yoshiyuki Miyamoto, Mutsuko Hatano, and Takayuki Iwasaki. Low-temperature spectroscopic investigation of lead-vacancy centers in diamond fabricated by high-pressure and high-temperature treatment. ACS Photonics, 8(10):2947–2954, 2021.

[14] G DAVIES and MF HAMER. Optical studies of 1.945 ev vibronic band in diamond. PROCEEDINGS OF THE ROYAL SOCIETY OF LONDON SERIES A-MATHEMATICAL AND PHYSICAL SCIENCES, 348(1653):285–298, 1976.

[15] Elke Neu, David Steinmetz, Janine Riedrich-Moeller, Stefan Gsell, Martin Fischer, Matthias Schreck, and Christoph Becher. Single photon emission from silicon-vacancy colour centres in chemical vapour deposition nano-diamonds on iridium. NEW JOURNAL OF PHYSICS, 13, FEB 21 2011.

[16] Takayuki Iwasaki, Fumitaka Ishibashi, Yoshiyuki Miyamoto, Yuki Doi, Satoshi Kobayashi, Takehide Miyazaki, Kosuke Tahara, Kay D. Jahnke, Lachlan J. Rogers, Boris Naydenov, Fedor Jelezko, Satoshi Yamasaki, Shinji Nagamachi, Toshiro Inubushi, Norikazu Mizuochi, and Mutsuko Hatano. Germanium-vacancy single color centers in diamond. SCIENTIFIC REPORTS, 5, AUG 7 2015.

[17] A. Batalov, C. Zierl, T. Gaebel, P. Neumann, I.-Y. Chan, G. Balasubramanian, P. R. Hemmer, F. Jelezko, and J. Wrachtrup. Temporal coherence of photons emitted by single nitrogen-vacancy defect centers in diamond using optical rabi-oscillations. Phys. Rev. Lett., 100:077401, Feb 2008.

[18] Yan Liu, Petr Siyushev, Youying Rong, Botao Wu, Liam Paul McGuinness, Fedor Jelezko, Syuto Tamura, Takashi Tanii, Tokuyuki Teraji, Shinobu Onoda, Takeshi Ohshima, Junichi Isoya, Takahiro Shinada, Heping Zeng, and E Wu. Investigation of the silicon vacancy color center for quantum key distribution. Opt. Express, 23(26):32961–32967, Dec 2015.

[19] M. K. Bhaskar, D. D. Sukachev, A. Sipahigil, R. E. Evans, M. J. Burek, C. T. Nguyen, L. J. Rogers, P. Siyushev, M. H. Metsch, H. Park, F. Jelezko, M. Lončar, and M. D. Lukin. Quantum nonlinear optics with a germanium-vacancy color center in a nanoscale diamond waveguide. Phys. Rev. Lett., 118:223603, May 2017.

[20] Martin Berthel, Oriane Mollet, Géraldine Dantelle, Thierry Gacoin, Serge Huant, and Aurélien Drezet. Photophysics of single nitrogen-vacancy centers in diamond nanocrystals. Phys. Rev. B, 91:035308, Jan 2015.

[21] Janine Riedrich-Moeller, Carsten Arend, Christoph Pauly, Frank Muecklich, Martin Fischer, Stefan Gsell, Matthias Schreck, and Christoph Becher. Deterministic coupling of a single silicon-vacancy color center to a photonic crystal cavity in diamond. NANO LETTERS, 14(9):5281–5287, SEP 2014.

[22] C. D. Clark, H. Kanda, I. Kiflawi, and G. Sittas. Silicon defects in diamond. Phys. Rev. B, 51:16681–16688, Jun 1995.

[23] Gopalakrishnan Balasubramanian, Philipp Neumann, Daniel Twitchen, Matthew Markham, Roman Kolesov, Norikazu Mizuochi, Junichi Isoya, Jocelyn Achard, Johannes Beck, Julia Tissler, Vincent Jacques, Philip R. Hemmer, Fedor Jelezko, and Joerg Wrachtrup. Ultralong spin coherence time in isotopically engineered diamond. NATURE MATERIALS, 8(5):383–387, MAY 2009.

[24] D. D. Sukachev, A. Sipahigil, C. T. Nguyen, M. K. Bhaskar, R. E. Evans, F. Jelezko, and M. D. Lukin. Silicon-vacancy spin qubit in diamond: A quantum memory exceeding 10 ms with single-shot state readout. Phys. Rev. Lett., 119:223602, Nov 2017.

[25] Petr Siyushev, Mathias H. Metsch, Aroosa Ijaz, Jan M. Binder, Mihir K. Bhaskar, Denis D. Sukachev, Alp Sipahigil, Ruffin E. Evans, Christian T. Nguyen, Mikhail D. Lukin, Philip R. Hemmer, Yuri N. Palyanov, Igor N. Kupriyanov, Yuri M. Borzdov, Lachlan J. Rogers, and Fedor Jelezko. Optical and microwave control of germanium-vacancy center spins in diamond. Phys. Rev. B, 96:081201, Aug 2017.

[26] A. Jarmola, V. M. Acosta, K. Jensen, S. Chemerisov, and D. Budker. Temperature- and magnetic-field-dependent longitudinal spin relaxation in nitrogen-vacancy ensembles in diamond. Phys. Rev. Lett., 108:197601, May 2012.

[27] Matthew E. Trusheim, Noel H. Wan, Kevin C. Chen, Christopher J. Ciccarino, Johannes Flick, Ravishankar Sundararaman, Girish Malladi, Eric Bersin, Michael Walsh, Benjamin Lienhard, Hassaram Bakhru, Prineha Narang, and Dirk Englund. Lead-related quantum emitters in diamond. Phys. Rev. B, 99:075430, Feb 2019.

[28] Gerg ő Thiering and Adam Gali. Ab initio magneto-optical spectrum of group-iv vacancy color centers in diamond. Phys. Rev. X, 8:021063, Jun 2018.

[29] Marc Sartison, Oscar Camacho Ibarra, Ioannis Caltzidis, Dirk Reuter, and Klaus D Jöns. Scalable integration of quantum emitters into photonic integrated circuits. Materials for Quantum Technology, 2(2):023002, jul 2022.

[30] Chiou-Fu Wang, Ronald Hanson, DD Awschalom, EL Hu, T Feygelson, J Yang, and JE Butler. Fabrication and characterization of two-dimensional photonic crystal microcavities in nanocrystalline diamond. Applied Physics Letters, 91(20):201112, 2007.

[31] R. Ishihara, J. Hermias, S. Yu, K. Y. Yu, Y. Li, S. Nur, T. Iwai, T. Miyatake, K. Kawaguchi, Y. Doi, and S. Sato. 3d integration technology for quantum computer based on diamond spin qubits. In 2021 IEEE International Electron Devices Meeting (IEDM), pages 14.5.1–14.5.4, 2021.

[32] Baris Bayram, Orhan Akar, and Tayfun Akin. Plasma-activated direct bonding of diamond-on-insulator wafers to thermal oxide grown silicon wafers. Diamond and Related Materials, 19(11):1431–1435, 2010.

[33] Noel H. Wan, Tsung-Ju Lu, Kevin C. Chen, Michael P. Walsh, Matthew E. Trusheim, Lorenzo De Santis, Eric A. Bersin, Isaac B. Harris, Sara L. Mouradian, Ian R. Christen, Edward S. Bielejec, and Dirk Englund. Large-scale integration of artificial atoms in hybrid photonic circuits. Nature, 583(7815):226–231, jul 2020.

[34] Shiyang Zhu and Guo-Qiang Lo. Aluminum nitride electro-optic phase shifter for backend integration on silicon. Optics express, 24(12):12501–12506, 2016.

[35] Zelin Hu, Linyun Long, Rongqiao Wan, Chen Zhang, Lei Zhang, Jianchang Yan, Huigao Duan, and Liancheng Wang. Ultrawide bandgap aln metasurfaces for ultraviolet focusing and routing. Optics Letters, 45(13):3466–3469, 2020.

[36] Smarak Maity, Linbo Shao, Stefan Bogdanović, Srujan Meesala, Young-Ik Sohn, Neil Sinclair, Benjamin Pingault, Michelle Chalupnik, Cleaven Chia, Lu Zheng, Keji Lai, and Marko Lončar. Coherent acoustic control of a single silicon vacancy spin in diamond. Nature Communications, 11(1):193, Jan 2020.

[37] Shiyang Zhu, Qize Zhong, Ting Hu, Yu Li, Zhengji Xu, Yuan Dong, and Navab Singh. Aluminum nitride ultralow loss waveguides and push-pull electro-optic modulators for near infrared and visible integrated photonics. In 2019 Optical Fiber Communications Conference and Exhibition (OFC), pages 1–3. IEEE, 2019.

[38] Zhaoyi Li, Zuowen Fan, Jingjie Zhou, Qingyu Cong, Xianfeng Zeng, Yumei Zhang, and Lianxi Jia. Process development of low-loss lpcvd silicon nitride waveguides on 8-inch wafer. Applied Sciences, 13(6), 2023.

[39] P. Knights Andrew T. Reed, Graham. Silicon photonics: an introduction. John Wiley & Sons, Ltd, 2004.

[40] Jia-ming Liu. Photonic Devices. Cambridge University Press, 2005.

[41] Piotr J Cegielski, Stephan Suckow, Anna Lena Giesecke, Caroline Porschatis, Holger Lerch, Maik Lütticke, Bartos Chmielak, and Max C Lemme. Silicon nitride waveguides and spot size converters with< 1.76 db loss over broad wavelength range from 1010 nm to 1110 nm for oct applications.

[42] Meng X Osgood, R. Jr. Principles of photonic integarted circuits. Springer Nature Switzerland AG, 2021.

[43] Milton A. F. Burns, W. K. Waveguide transitions and junctions. Springer Berlin Heidelberg, 1988.

[44] Wim Bogaerts, Pieter Dumon, Dries Van Thourhout, and Roel Baets. Low-loss, low-cross-talk crossings for silicon-on-insulator nanophotonic waveguides. Opt. Lett., 32(19):2801–2803, Oct 2007.

[45]

[46] HGFYRW Windischmann, Glenn F Epps, Yue Cong, and RW Collins. Intrinsic stress in diamond films prepared by microwave plasma cvd. Journal of Applied Physics, 69(4):2231–2237, 1991.

[47] Eiji Iwase, Pui-Chuen Hui, David Woolf, Alejandro W Rodriguez, Steven G Johnson, Federico Capasso, and Marko Lončar. Control of buckling in large micromembranes using engineered support structures. Journal of Micromechanics and Microengineering, 22(6):065028, 2012.

[48] I Bayn, S Mouradian, L Li, JA Goldstein, T Schröder, J Zheng, EH Chen, O Gaathon, M Lu, A Stein, et al. Fabrication of triangular nanobeam waveguide networks in bulk diamond using single-crystal silicon hard masks. Applied Physics Letters, 105(21):211101, 2014.

[49] Sailong Wu, Xin Mu, Lirong Cheng, Simei Mao, and H.Y. Fu. State-of-the-art and perspectives on silicon waveguide crossings: A review. Micromachines, 11(3), 2020.

[50] Yangjin Ma, Yi Zhang, Shuyu Yang, Ari Novack, Ran Ding, Andy Eu-Jin Lim, Guo-Qiang Lo, Tom Baehr-Jones, and Michael Hochberg. Ultralow loss single layer submicron silicon waveguide crossing for soi optical interconnect. Opt. Express, 21(24):29374–29382, Dec 2013.

[51] P. Sanchis, J. V. Galan, A. Griol, J. Marti, M. A. Piqueras, and J. M. Perdigues. Low-crosstalk in silicon-on-insulator waveguide crossings with optimized-angle. IEEE Photonics Technology Letters, 19(20):1583–1585, 2007.

[52] L.B. Soldano and E.C.M. Pennings. Optical multi-mode interference devices based on self-imaging: principles and applications. Journal of Lightwave Technology, 13(4):615–627, 1995.

[53] Trung-Thanh Le and Duy-Tien Le. Multimode waveguides on an soi platform for arbitrary power splitting ratio couplers. In Kok Yeow You, editor, Emerging Waveguide Technology, chapter 12. IntechOpen, Rijeka, 2018.

[54] M. Bachmann, P. A. Besse, and H. Melchior. General self-imaging properties in n × n multimode interference couplers including phase relations. Appl. Opt., 33(18):3905–3911, Jun 1994.

[55] Simon Gröblacher, Jeff T. Hill, Amir H. Safavi-Naeini, Jasper Chan, and Oskar Painter. Highly efficient coupling from an optical fiber to a nanoscale silicon optomechanical cavity. Applied Physics Letters, 103(18):181104, 2013.

[56] Heliang Liu, Hwayaw Tam, P.K.A. Wai, and Edwin Pun. Low-loss waveguide crossing using a multimode interference structure. Optics Communications, 241(1):99–104, 2004.

[57] Noel H. Wan, Tsung-Ju Lu, Kevin C. Chen, Michael P. Walsh, Matthew E. Trusheim, Lorenzo De Santis, Eric A. Bersin, Isaac B. Harris, Sara L. Mouradian, Ian R. Christen, Edward S. Bielejec, and Dirk Englund. Large-scale integration of artificial atoms in hybrid photonic circuits. Nature, 583(7815):226–231, Jul 2020.

[58] Elly Gil, JB Park, JS Oh, and GY Yeom. Characteristics of siox thin films deposited by atmospheric pressure chemical vapor deposition as a function of hmds/o2 flow rate. Thin Solid Films, 518(22):6403–6407, 2010.

[59] Sara L. Mouradian, Tim Schröder, Carl B. Poitras, Luozhou Li, Jordan Goldstein, Edward H. Chen, Jaime Cardenas, Matthew L. Markham, Daniel J. Twitchen, Michal Lipson, and Dirk Englund. Scalable integration of long-lived quantum memories into a photonic circuit, 2014.

A

Taper Profile Simulation Results

Tapered adiabatic couplers come in different geometries as illustrated in fig. 3.6. The main downside to adiabatic couplers is the required length being too long to satisfy the adiabaticity criterion. This results in a larger footprint when compared to other couplers. Therefore, it is worthwhile to investigate the taper profile at which lower lengths are required for the same performance.

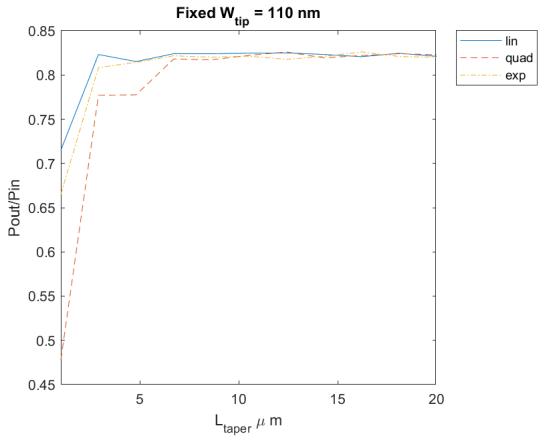

Figure A.1: Normalized transmission of linear, quadratic and exponential profiles as a function of taper length

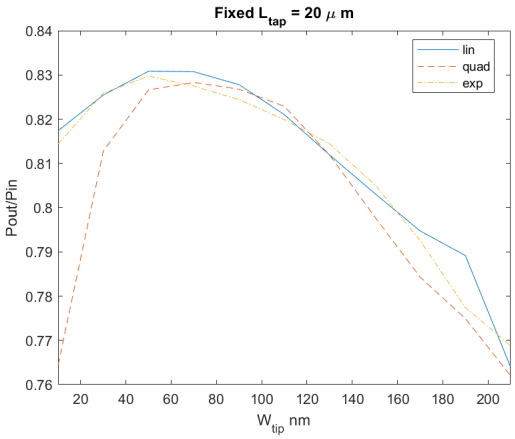

Figure A.2: Normalized transmission of linear, quadratic and exponential profiles as a function of tip width

The three profiles shown in fig. 3.6 have been simulated using beam propagation method (BPM). While FDTD simulation is the most accurate for simulating 3D structures, however, it sets very high requirement on the computational resources. Given that the purpose of these simulations is to only gain insight in these taper profiles and not strictly design or verify, then using BPM is sufficient. The simulations have been verified using FDTD method as will be shown later in fig. A.9. Insertion loss of different profiles at different taper lengths and tip widths have been simulated in BPM. The coupling efficiency has been simulated as well. These simulations have been done for $800nm$ waveguide width and $200nm$ thickness.

Figure A.2 shows the normalized transmission as a function of tip width at $20\mu m$ taper length, long enough to ensure adiabatic coupling. The figure shows and optimum tip width range $50 \leq W_{tip} \leq 100nm$ at which the transmission is highest for the linear profile. The optimum range for the quadratic taper shifts by roughly $10nm$ higher, whereas exponential optimum range shifts with $10nm$ lower. The linear profile shows the highest transmission followed by exponential and quadratic. This is as expected due to the linear taper being the most adiabatic when compared with non-linear profile.

As for the coupling efficiency, similar optimum tip width range can be observed from fig. A.6. Beyond this optimum, exponential profile yields higher coupling efficiency. This means that the mode field profile still matches relatively well with that of the single mode waveguide at large tip widths, though at the expense of higher scattering and thus higher losses.

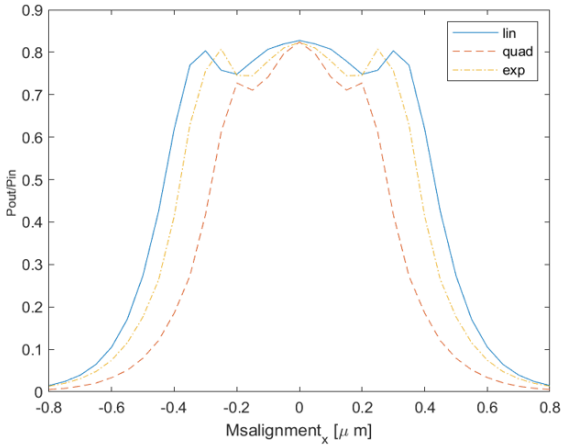

Figure A.3: Normalized transmission of linear, quadratic and exponential profiles as a function of misalignment in x direction.

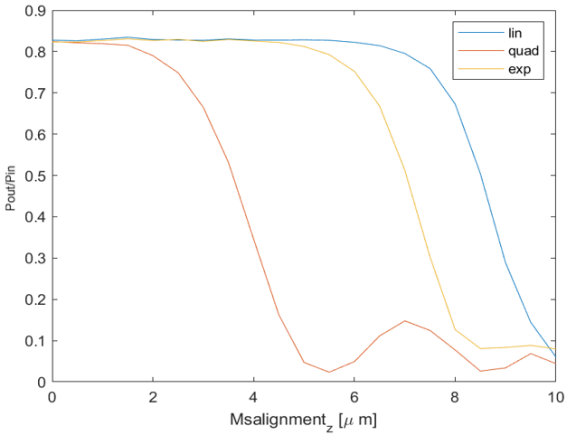

Figure A.4: Normalized transmission of linear, quadratic and exponential profiles as a function of misalignment in z direction.

As for the taper length, fig. A.1 shows that the transmission is highest for the linear taper followed by exponential and quadratic for the same taper length. For the same transmission, linear and exponential profiles require lowest taper lengths followed by quadratic. The transmission remains constant for all tapers for $L_{tap} \geq 6\mu m$ for which losses are dominated by propagation losses. As for the coupling efficiency, the exponential profile shows higher coupling efficiency at a lower length fig. A.5 when compared to the other profiles.

Misalignment simulations are shown in figs. A.3 and A.4 for the misalignment in x and z direction respectively. As the misalignment increases, the transmission decreases for all profiles. However, at a certain misalignment, the transmission slightly increases despite the increased misalignment. This is attributed to the coupling of the evanescent fields as the tapers are in the vicinity of each other at this misalignment. Linear profile shows the highest misalignment tolerance, followed by exponential and quadratic. At first glans, this can be attributed to the linear profile showing the highest transmission at 0 misalignment. However, this is not the only explanation, as the higher transmission can be observed at higher misalignment as well. This is attributed to the taper profile allowing for higher evanescent coupling as the width of the taper decreases at a slower rate when compared with non-linear profiles. This explains why the transmission peak at higher misalignment occurs at lower misalignment value for non-linear profiles. This is further observed in fig. A.7 where the field mode match increases at higher misalignment after it drops dramatically.
As for the misalignment in z direction, all profiles show similar behavior where the transmission abruptly drops. The linear taper profile shows the highest misalignment in the z direction as well.

FDTD verification simulation is shown in fig. A.9 for $10\mu m$ taper length and $100nm$ tip width for which the transmission is 97% and the coupling efficiency is 99%.

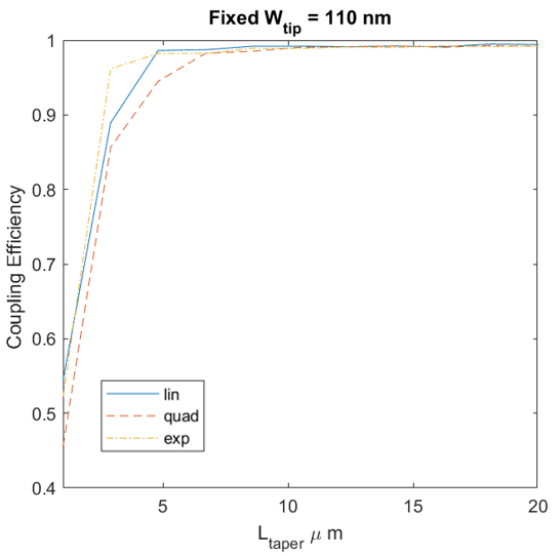

Figure A.5: Coupling efficiency of linear, quadratic and exponential profiles as a function of taper length

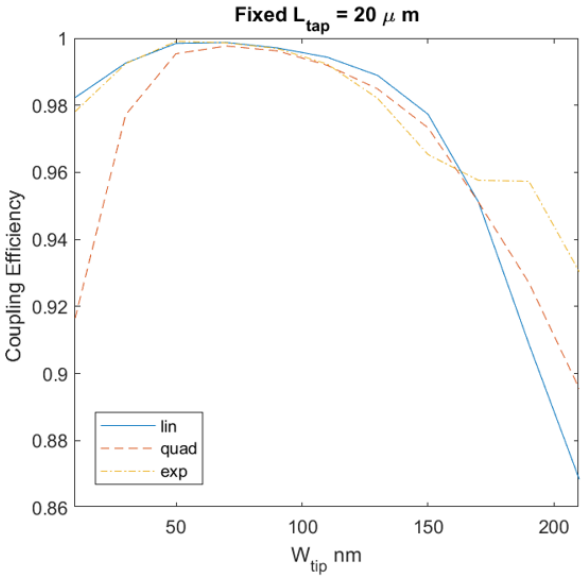

Figure A.6: Coupling efficiency of linear, quadratic and exponential profiles as a function of tip width.

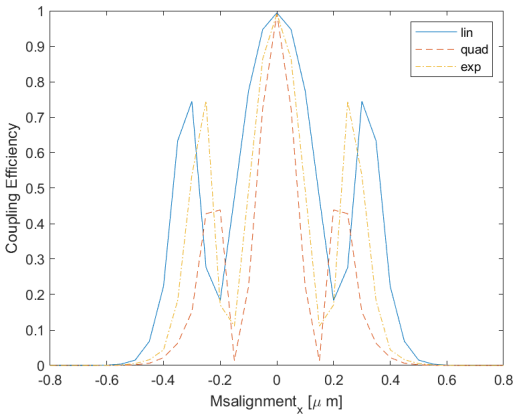

Figure A.7: Coupling efficiency of linear, quadratic and exponential profiles as a function of misalignment in x direction.

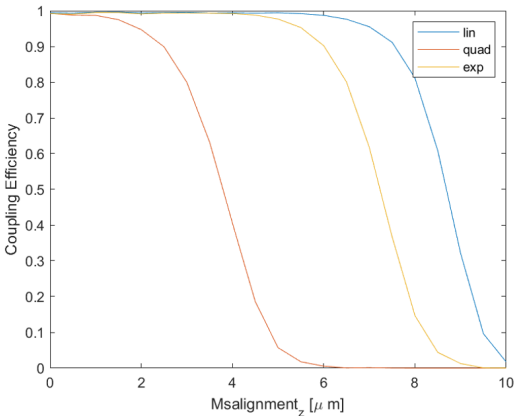

Figure A.8: Coupling efficiency of linear, quadratic and exponential profiles as a function of misalignment in z direction

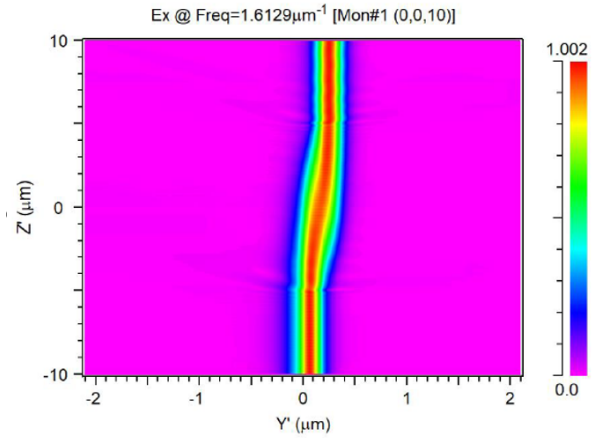

Figure A.9: FDTD simulation of the mode propagating from the bottom waveguide to the top waveguide.

B

MMI Mode Propagation: Additional results

FDTD simulation has been done on the designed MMI. The field mode profile of the mode as it propagates through the MMI are shown in the figures below. This demonstrates the expected self-imaging effect where the input mode is replicated at the center of the MMI and then again at the output of the MMI.

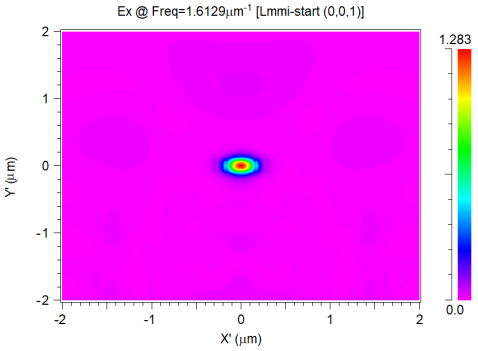

Figure B.1: The field mode profile at the input of the MMI. Note that the evanescent field is due to compromised confinement.

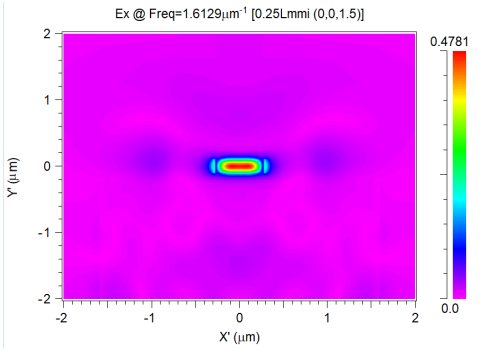

Figure B.2: The field mode profile at $0.25Lmmi$ which is wider due to the modes interfering with each other

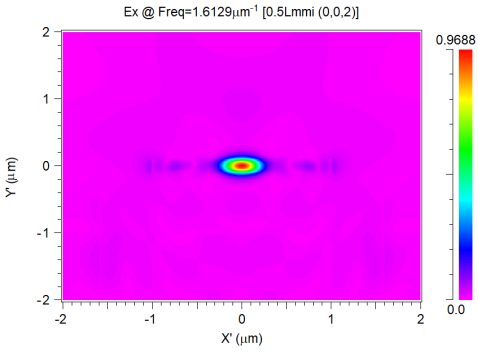

Figure B.3: The field mode profile at $0.5Lmmi$ at which the input mode is replicated, demonstrating the self-imaging effect.

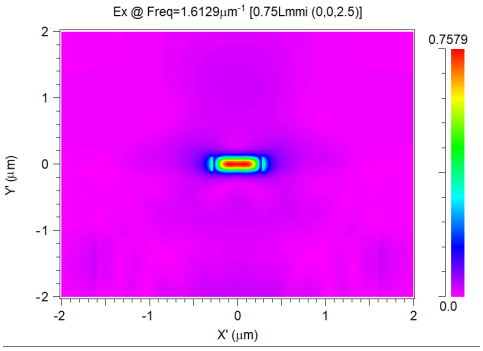

Figure B.4: The field mode profile at $0.75Lmmi$ repeating the same profile as in $0.25Lmmi$.

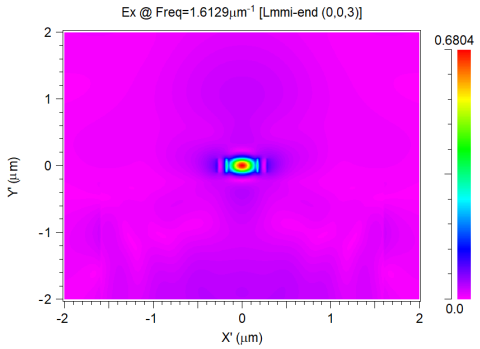

Figure B.5: The field mode profile at the output of the MMI / input of the single mode waveguide showing the replicated field mode profile.

C

Stress analysis of used diamond donor chiplets

As mentioned in the original text, the magnitude of the stress is overestimated as the model is rigidly defined. However, the results can be useful in understanding the stress distribution in the structure. The simulations show no significant difference of the stress distribution across the chiplet. The only difference is in the stress profile is at the attachment points shown in fig. C.1, figs. C.2 and C.3. As expected, the maximum and minimum stress are concentrated on the tethers for chiplets $T-10-100$ and $H-10-100$ as shown in figs. C.2 and C.3. This indicates that these structures can be easily released from the wafer. As for the stress distribution across the chiplet,

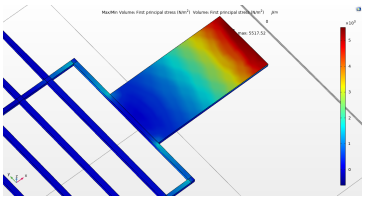

Figure C.1: Stress analysis for chiplet $B-10-100$.

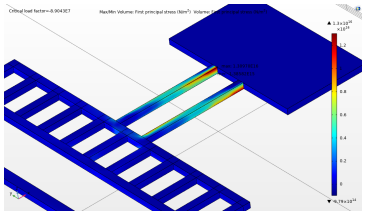

Figure C.2: Stress analysis for chiplet $T-10-100$.

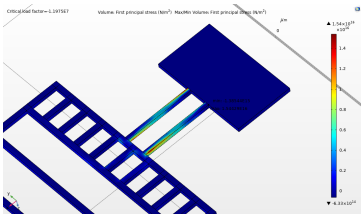

Figure C.3: Stress analysis for chiplet $H-10-100$.